

ABSTRACT

BISHOP, JASON THOMAS. Development of a Wind Tunnel Test Cell for Small Propellers with Application to the Plank Unmanned Aerial Vehicle. (Under the direction of Dr. Charles E. Hall Jr.).

The Plank unmanned aerial vehicle has been designed to be a test platform for an experimental bias angular momentum flywheel designed by the NASA Guidance and Controls Branch. The baseline configuration of the aircraft is a flying wing with zero quarter-chord sweep. The benefits of this type of configuration include low structural weight and complexity and reduced drag compared to a standard wing-tail configuration. However, this type of configuration is inherently sensitive to pitch disturbances due to low pitch damping and moment of inertia. In order to remedy this sensitivity, NASA has proposed the use of a bias angular momentum flywheel with its rotational axis aligned with the z-axis of the aircraft. This momentum wheel will effectively stiffen the pitch axis of the aircraft by coupling it with the high damping, high moment of inertia roll axis.

The aircraft was designed to be re-configurable allowing for a variety of flying qualities ranging from a well-behaved wing and aft tail configuration to the much more sensitive flying wing configuration. This range of flying qualities will allow for a more comprehensive performance evaluation of the momentum wheel system as well as contribute to risk mitigation during initial flight tests.

An electric propulsion system has been chosen for this aircraft due its simple operation and low vibration characteristics. The AXi 5330/18 motor was chosen along with a Castle Creations Phoenix HV-110 electronic speed control. The system is powered by three FlightPower 5000 mAh 10s Evo Lite battery packs connected in parallel. A four-bladed propeller configuration was used in order to absorb the necessary power from the motor while still fitting between the tail booms of the aircraft.

In order to experimentally evaluate the performance of the Plank propulsion system in the NCSU Subsonic Wind Tunnel, the Propeller Test Cell (PTC) was developed. The PTC consists of a strain

gage based load cell that measures the thrust and torque generated by the propulsion system along with system operating conditions such as current, voltage, RPM, motor temperature, and battery consumption. The PTC was used to characterize the performance of three candidate propellers for the Plank aircraft: 16x10, 17x8, and 17x10. With this data, certain propulsion specific performance parameters of the aircraft were calculated including thrust and power available, rate of climb and climb angle, range, endurance, and take off performance. After analyzing the performance for each of the three propellers, the 17x8 propeller produced the most desired aircraft performance and was chosen to be paired with the AXi motor and the Plank aircraft.

Development of a Wind Tunnel Test Cell for Small Propellers with Application to the Plank
Unmanned Aerial Vehicle

by
Jason Thomas Bishop

A thesis submitted to the Graduate Faculty of
North Carolina State University
in partial fulfillment of the
requirements for the degree of
Master of Science

Aerospace Engineering

Raleigh, North Carolina

2009

APPROVED BY:

Dr. Charles E. Hall Jr.
Committee Chair

Dr. Ashok Gopalarathnam

Dr. Pierre A. Gremaud

DEDICATION

This work in its entirety is dedicated to my wife and best friend, Leigh Bishop. Leigh, you have been my girlfriend, my fiancé, and my wife all within the span of this research. You have made countless sacrifices in the interest of this research and in the interest of my success. You have dealt with my constant physical and mental unavailability, put up with my increasing amount of pity-parties, and accommodated the always unforeseen schedule change. Most impressively, in spite of all these things, you have remained a never-failing source of encouragement and confidence. You believed in me when I lost hope, you encouraged me whenever I faltered, and you were a constant and much-needed voice of reason and reality to help me find my path when I got lost. Any and all success in this research is as much yours as it is mine. There is no question in my mind that this document and this degree would not exist if it were not for your presence in my life. As much of a blessing as you have been throughout this research, you have been even more so throughout our five years together. A simple 'thank you' will not suffice; I am forever in debt to you for your selflessness and unwavering devotion. I love you, Leigh.

BIOGRAPHY

Jason Bishop was born in 1984 in Minnesota to Kim and Peter Bishop. He has two younger brothers, Justin and Adam. He moved with his family to North Carolina in 1994, and was a 2002 graduate of Green Hope High School in Cary, NC. That fall, Jason began his studies in Aerospace Engineering at North Carolina State University; he graduated Cum Laude with a Bachelors Degree in 2007. After graduation, he immediately began his graduate work, with a focus on airworthiness of small unmanned aerial systems. After two semesters, the Flight Research Group began work with the Guidance and Controls Branch at NASA Langley to design, construct, and flight test an unmanned aerial system. Jason became the lead graduate student on this project and based his research on the propulsion system design and testing for the aircraft. Jason currently resides in Raleigh with his wife, Leigh.

ACKNOWLEDGMENTS

I would like take this opportunity to first thank my advisor Dr. Charles Hall. His advice, expectations, and confidence have been invaluable throughout my graduate career. He has provided me with countless opportunities to further my knowledge and gain experience as an engineer, which has contributed to the success of this research and will continue to contribute to my success in future endeavors. I would also like to thank my committee members, Dr. Ashok Gopalarathnam and Dr. Pierre Gremaud, for everything that they have taught me throughout my undergraduate and graduate career and for their support in regards to this research.

I want to give a special thanks to my family. Mom and Dad, thank you for your financial support throughout my undergraduate career and for all of the sacrifices you have made so that I could have the opportunity to go to the college of my choice. More importantly, thank you for your emotional support and encouragement. You both have had a lot of confidence in me throughout the years, which has driven me to strive for success in both school and life. To Justin and Adam: you guys have become such great friends to me, in addition to brothers. I can always count on hilarious antics when the three of us are together. I always looked forward to hanging out with you guys on the weekends; it ended up being such a valuable break from the rigors of grad school, and I would have gone insane otherwise.

I also want to thank Stearns Heinzen for his invaluable guidance and advice. He has been an excellent mentor, role model, and friend throughout my graduate career. Any time I had a question about my research, my school work, or life in general, I could always count on Stearns to provide voice of both knowledge and reason (and sometimes sarcasm, but hey, that's how you learn). I am a better engineer, person, and swimmer for knowing him.

And to all the guys in the Langley room: being around such a sharp group of guys for two years has definitely made me a better engineer. The advice, teachings, criticism, support, sarcasm, laughter, lunches, intramural teams, triathlons, flash games, FailBlog, and whirly-birds all contributed to such a wonderful work environment that I will forever reflect on while I sit in the cubicle at my future job.

I want to specifically thank Trent Young and Lars Soltmann who helped out with wind tunnel testing while I had the flu; you guys are life-savers.

Special thanks go to the Guidance and Controls Group at NASA Langley, specifically Dan Moerder, for the opportunity to work on the Plank project and for funding this research.

TABLE OF CONTENTS

LIST OF TABLES.....	viii
LIST OF FIGURES.....	ix
NOMENCLATURE.....	xi
1. INTRODUCTION.....	1
2. AIRCRAFT CONFIGURATION.....	2
2.1 Fuselage.....	2
2.2 Wing.....	4
2.3 Wing-Fuselage Joint.....	6
2.4 Empennage.....	8
2.5 Momentum Wheel Mounting.....	10
2.6 Hatches.....	11
2.7 Landing Gear.....	14
2.8 Mass Properties.....	16
3. PROPULSION SYSTEM DESIGN.....	17
3.1 System Selection.....	17
3.2 Motor selection.....	17
3.3 Speed Control Selection.....	18
3.4 Battery Selection.....	19
3.5 Propeller Selection.....	20
3.6 System Configuration.....	21
3.7 Propulsion System Wiring.....	25
4. PROPELLER TEST CELL DEVELOPMENT.....	26
4.1 Configuration.....	27
4.2 Material Selection.....	28
4.3 Load Cell Sizing.....	28
4.4 Load Cell Integration.....	29
4.5 ANSYS Analysis.....	30

4.6 Strain Gage Bridge Configuration	34
4.7 Constructed PTC	38
4.8 Calibration.....	39
4.9 Signal Noise	43
5. WIND TUNNEL TESTING.....	48
5.1 Equipment.....	48
5.2 Experiment Procedure	49
5.3 Data Reduction.....	50
5.3.1 Temperature Correction	50
5.3.2 Blockage Correction.....	50
5.4 Results.....	51
5.4.1 Propeller Data.....	51
5.4.2 Thrust and Power Available.....	55
6. AIRCRAFT PERFORMANCE ANALYSIS.....	59
6.1 Parasite Drag Estimation.....	59
6.2 Thrust and Power Required	60
6.3 Rate of Climb.....	62
6.4 Range and Endurance	64
6.5 Takeoff Performance	66
6.6 Propeller Selection	68
7. CONCLUSION.....	69
8. FUTURE WORK	70
REFERENCES.....	71
APPENDICES.....	72
Appendix A: Calibration Run Schedule	73
Appendix B: Wind Tunnel Data	76
Appendix C: Take Off MATLAB Code (Takeoff_Master.m)	81

LIST OF TABLES

Table 1: Moments and Products of Inertia.....	16
Table 2: AXi 5330/18 Motor Specifications ¹	18
Table 3: Phoenix HV-110 Speed Control Specifications ²	19
Table 4: Load Cell Candidate Material Properties ³	28
Table 5: Load Cell Design and Limit Load Values.....	31
Table 6: Strain Gage Specs for Thrust Specific Gages (EA-13-031DE-350/E) ⁴	35
Table 7: Strain Gage Specs for Thrust Specific Gages (EA-13-060LZ-120/E) ⁵	35
Table 8: Significance Indicators for Calibration Model Effects.....	41
Table 9: Calibration Model with Motor Assembly Weight.....	42
Table 10: Calibration Model without Motor Assembly Weight.....	42
Table 11: Model Uncertainties with and without Motor Assembly Weight.....	42
Table 12: Component Parasite Drag Contributions.....	59
Table 13: Electrical System Efficiency.....	64
Table 14: Maximum Range Operating Conditions.....	65
Table 15: Maximum Range.....	66
Table 16: Maximum Endurance.....	66
Table 17: Takeoff Rotation Distances and Velocities.....	67
Table 18: Aircraft Performance Summary with 17x8 Propeller.....	68
Table 19: Calibration Run Schedule.....	73
Table 20: 16x10 Propeller Data.....	76
Table 21: 17x8 Wind Tunnel Data.....	77
Table 22: 17x10 Wind Tunnel Data.....	79

LIST OF FIGURES

Figure 1: The Plank Aircraft	2
Figure 2: Fuselage Internal Structure Layout.....	3
Figure 3: Wing Internal Structure Configuration	4
Figure 4: Control Surface Configuration.....	5
Figure 5: Drag Rudder Functionality: (a) Directional Control, (b) Drag Brakes.....	5
Figure 6: Wing-Fuselage Joiner Assembly	6
Figure 7: Aft Wing-Fuselage Joiner Assembly.....	7
Figure 8: Wing-Fuselage Leading Edge Joiner Tabs.....	8
Figure 9: Tail Configurations: (a) Flying Wing Configuration, (b) Intermediate Tail Configuration, (c) Aft Tail Configuration	9
Figure 10: Vertical Tail Configuration.....	10
Figure 11: Momentum Wheel Mounting Configuration	10
Figure 12: Momentum Wheel Pitch Angle Range: (a) +15°, (b) 0°, (c) -15°.....	11
Figure 13: Fuselage Hatch Layout	12
Figure 14: Wing Hatch Layout.....	13
Figure 15: Landing Gear Configuration	14
Figure 16: Nose Gear Mount	14
Figure 17: Main Gear Mount	15
Figure 18: AXI 5330/18 Motor ¹	18
Figure 19: Phoenix HV-110 Brushless Motor Controller ²	19
Figure 20: FlightPower Evo F3A Battery	20
Figure 21: Zinger 4-Blade Pusher Propeller	21
Figure 22: Propulsion System Layout	22
Figure 23: Battery Tray	23
Figure 24: Motor Cooling Inlet.....	24
Figure 25: Propulsion System Wiring Harness Layout.....	25
Figure 26: PTC Load Cell	27

Figure 27: Propeller Test Cell Assembly	29
Figure 28: ANSYS Model of Propeller Test Cell Assembly	30
Figure 29: Strain Intensity Plot for Load Cell under Design Thrust Load (20 lbs)	31
Figure 30: Strain Intensity Plot for Load Cell under Design Torque Load.....	32
Figure 31: Strain Intensity Plot for Load Cell under Design Thrust Load and Design Torque Load	33
Figure 32: Stress Intensity Plot for Load Cell under Limit Thrust Load and Limit Torque Load.....	34
Figure 33: (a) Torque Gage Designation; (b) Thrust Gage Designation.....	36
Figure 34: Thrust Bridge Circuit Diagram	37
Figure 35: Torque Bridge Circuit Diagram	37
Figure 36: Propeller Test Cell with Motor Adapter Removed	38
Figure 37: Propeller Test Cell with AXi 5330/18 Attached	39
Figure 38: Propeller Test Cell with Shroud Mounted on Wind Tunnel Sting.....	39
Figure 39: PTC with Calibration Bar attached.....	40
Figure 40: Power Spectrum Analysis of Motor RPM Progression through Resonance.....	44
Figure 41: FFT Analysis for Thrust Impulse on PTC	45
Figure 42: FFT Analysis for Torque Impulse on PTC	46
Figure 43: Medusa Power Analyzer Pro	48
Figure 44: Propeller Thrust Coefficient	52
Figure 45: Propeller Power Coefficient	52
Figure 46: Propeller Efficiency	53
Figure 47: Propeller Speed-Power Coefficient.....	54
Figure 48: Torque for 17x10 Propeller	56
Figure 49: Thrust Available	57
Figure 50: Power Available.....	58
Figure 51: Thrust Required and Available	60
Figure 52: Power Required and Available	61
Figure 53: Rate of Climb	62
Figure 54: Climb Angle.....	63

NOMENCLATURE

A	propeller disk area
C	wing tunnel test section area
C_{batt}	battery energy capacity
C_D	drag coefficient
C_L	lift coefficient
c_p	propeller power coefficient
c_s	propeller speed-power coefficient
c_t	propeller thrust coefficient
d	propeller diameter
ESC	electronic speed control
I_{xx}	x-axis moment of inertia
I_{yy}	y-axis moment of inertia
I_{zz}	z-axis moment of inertia
I_{xy}	x-y product of inertia
I_{yz}	y-z product of inertia
I_{xz}	x-z product of inertia
i	motor current
i_0	motor no load current
J	propeller advance ratio
k	spring constant
K_q	motor torque coefficient
K_v	motor speed coefficient
m	mass

n	propeller revolutions per second
P	power
P_A	power available
P_R	power required
PTC	propeller test cell
Q	torque
R/C	rate of climb
RPM	revolutions per minute
t	time
T	thrust
V	velocity
V'	corrected velocity
W	weight
γ	climb angle
η	efficiency
ρ	atmospheric density
Ω	angular velocity
ω_n	undamped natural frequency

1. INTRODUCTION:

The Guidance and Controls Branch from NASA has tasked the Flight Research Group at NC State University to design and construct a remotely piloted vehicle (RPV) to serve as a test platform for an experimental stability augmentation system. The base configuration of the aircraft must be an unswept flying wing weighing no more than 60 pounds. The aircraft must also possess a reconfigurable empennage assembly for risk mitigation and to allow for adjustability of the flying qualities of the aircraft. Initial flight verification and testing will also be performed by Flight Research.

While an unswept flying wing configuration offers lower structural weight and complexity and lower drag compared to a conventional configuration, this type of configuration is inherently sensitive to pitch disturbances due its low moment of inertia about the pitch axis. To remedy this issue, an angular momentum bias flywheel is employed with its axis of rotation aligned with the z-axis of the aircraft. This system will couple the sensitive pitch axis with the significantly less sensitive roll axis effectively stiffening the pitch characteristics of the aircraft.

An aircraft has been designed to meet these customer specifications. The platform has been given the nickname 'Plank' due to its baseline configuration of a plank flying wing. This research focuses on the design and testing of the Plank propulsion system. An electrical propulsion system has been selected due to its low vibration characteristics and ease of operation. An AXi 5330/18 brushless electric motor will be used with a 4-blade propeller pusher configuration. In order to test this propulsion system in the NCSU Subsonic Wind Tunnel, the Propeller Test Cell (PTC) was developed. The PTC is designed with a strain gage based load cell that measures the thrust and torque generated by the system. The PTC also has instrumentation to monitor and record the operating conditions of the motor (current, voltage, RPM, battery consumption, etc.). Three different propellers (16x10, 17x8, and 17x10) have been tested, along with the AXi motor, using the PTC. The aircraft performance using each of the three propellers has been calculated in order to determine the best fit for this application.

2. AIRCRAFT CONFIGURATION:

Other than the customer requirements, the driving factors of the design process include accessibility, ease of re-configurability, manufacturability, and portability. To ensure that the aircraft is easily re-configurable and has adequate accessibility for maintenance, assembly, and inspection, a CAD model of the aircraft has been created. The SolidWorks solid modeling package was used to model the various components of the aircraft, determine proper weight balance and component placement, and estimate the mass properties of the various configurations.

2.1 Fuselage

The fuselage is designed to contain the required internal volume to house the necessary flight components while still possessing adequate accessibility and a low drag profile. The profile of the fuselage utilizes a thicker version of the wing airfoil at the centerline and blends outward to the wing joint. This design exhibits a smooth transition from fuselage to wing reducing interference drag between the two bodies. The airfoil cross-section of the fuselage acts to reduce the profile drag of the body while also allowing the fuselage to contribute to the overall lift of the aircraft.

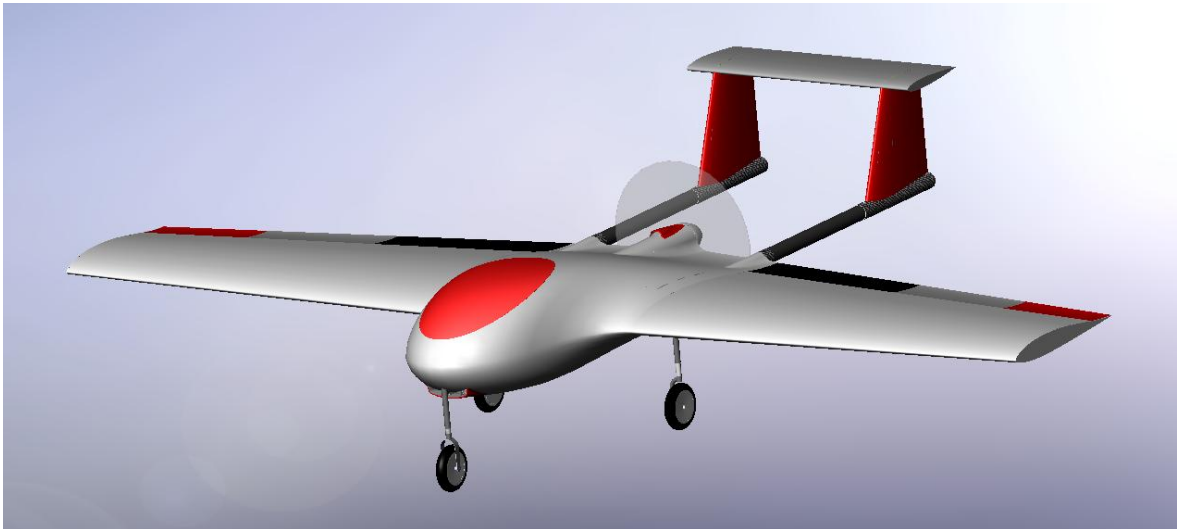


Figure 1: The Plank Aircraft

The fuselage is extended 18 inches ahead of the wing root leading edge to allow for component placement forward of the neutral point to correctly place the center of gravity of the aircraft. The

height of the fuselage has been chosen in order to meet internal volume requirements specified by the customer.

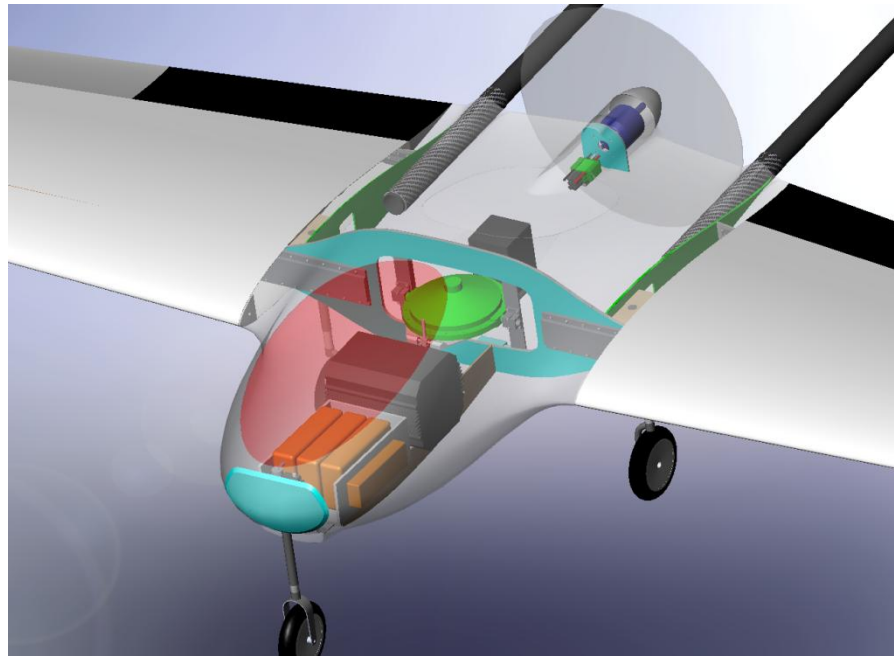


Figure 2: Fuselage Internal Structure Layout

The fuselage internal structure consists of three bulkheads (blue) and two ribs (green). The major structural element of the fuselage is the main bulkhead which is located such that it is aligned with the quarter chord of the wing. This bulkhead is responsible for transferring loads from the wings as well as loads to and from the momentum wheel. It also plays a major role in supporting landing loads from the main gear. There is a bulkhead located in the nose of the aircraft to which the nose gear assembly will be mounted. The motor will be mounted to a third bulkhead in the rear of the fuselage.

There are two ribs in the fuselage located adjacent to the fuselage wing joint. These ribs are responsible for securing and supporting the loads from the tail boom sockets and main gear mounts. The ribs also provide additional rigidity to the skin in the region of the wing joint ensuring that the joint maintains a proper shape.

2.2 Wing

The wing configuration is designed to meet the customer requirement of a zero sweep, plank wing. The wing structure utilizes a monocoque design with a hollow composite skin and composite supporting structure. The skin along with the internal structure is designed to support all possible load scenarios within the flight regime as well as provide mounting locations for control surface actuators and pass-through holes for wiring.

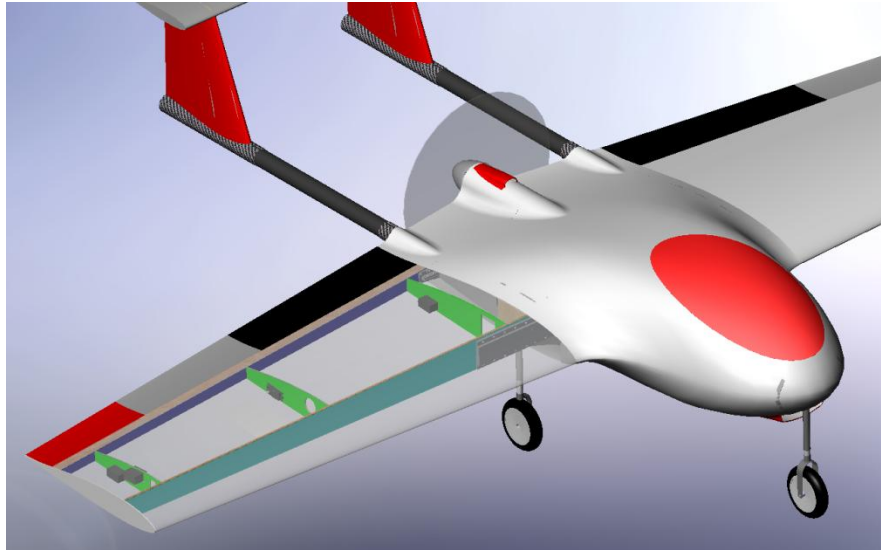


Figure 3: Wing Internal Structure Configuration

The major structural element in the wing is the main wing spar (blue). This spar is located at the quarter chord of the wing and is constructed out of $\frac{1}{4}$ inch cross-grain balsa with 8 ounce fiberglass laminated on the front and back faces. The main spar will be responsible for transferring the majority of the flight loads from the wing to the fuselage. The aft most spar in the wing (purple) is designed to support the torsional loads on the wing and also serve as a mounting point for the control surface hinges.

The wing also contains three ribs (green) that span the distance between the main spar and the aft spar. These ribs are responsible for supporting torsional loads on the wing and are designed to be constructed out of $\frac{1}{8}$ inch birch plywood. Each rib will also serve as a mounting point for the control surface servos and possess cutouts for wire routing and component access.

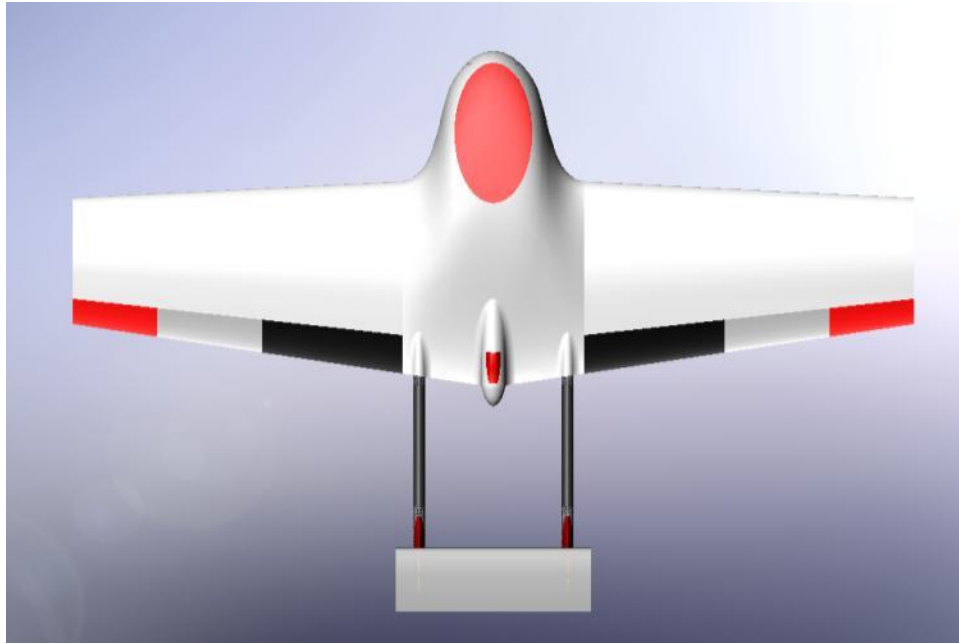


Figure 4: Control Surface Configuration

There are three control surfaces located on each wing. These control surfaces are 20 percent of the wing chord and have spans of 20, 15, and 12 inches for the inboard, middle, and outboard control surfaces respectively. Each control surface is designed with the ability to function as elevons (ailerons and elevators) to provide pitch and roll control. Additionally, the outboard control surfaces are designed to function as drag rudders in order to supply directional control and aerodynamic braking.

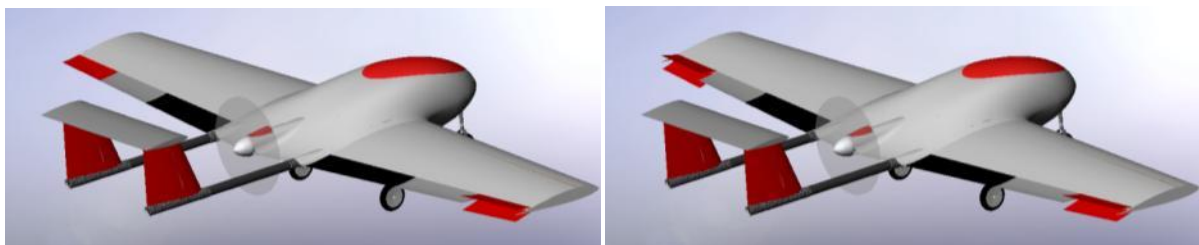


Figure 5: Drag Rudder Functionality: (a) Directional Control, (b) Drag Brakes

The control surfaces are actuated using internally located servos through a pushrod and control horn linkage. The control linkages for the inboard two surfaces exit the wing skin on the lower

surface in order to not disrupt the airflow over the comparatively more aerodynamically sensitive upper surface. The linkages for the drag rudders exit on the top and bottom surface of the wing skin for the upper and lower drag rudder surfaces.

2.3 Wing-Fuselage Joint

Due to the size of the aircraft, the wings are designed to be removable to allow for ease of transportation as well as access to internal components. The design of the wing joint is critical as it is responsible for transferring all of the flight loads from the wing panels to the center section. A blade and socket configuration has been designed to structurally join the main wing spar to the main fuselage bulkhead.

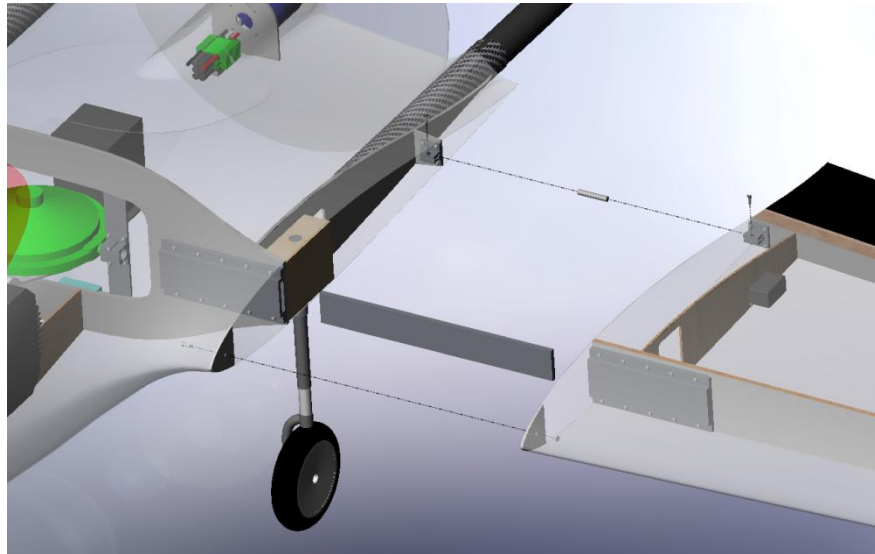


Figure 6: Wing-Fuselage Joiner Assembly

The socket consists of two parts to provide easier machinability: a channel that is designed to accept the blade, and a backplate to ensure a slip fit and protect the surface of the structure from scratching due to repeated assembly and disassembly. The blade is 12 inches long, 1.5 inches wide, and 0.25 inches thick with 6 inches inserted into each socket. Both the blade and the socket components are designed to be constructed out of 2024 Aluminum. The sockets are secured to the airframe using 6-32 hex head bolts. The blade is secured solely by the slip fit with the socket; this prevents requiring any holes or slots in the blade that may weaken the piece. The sockets are also

designed to be interchangeable between the wing and fuselage and both the sockets and the blade are interchangeable between the left and right sides of the aircraft.

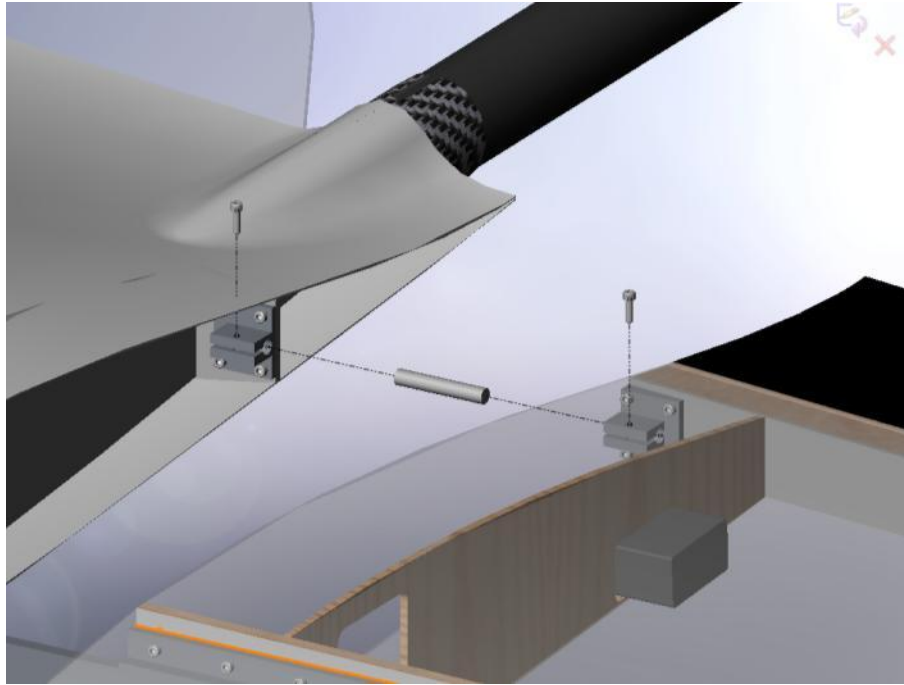


Figure 7: Aft Wing-Fuselage Joiner Assembly

The aft joiner assembly is designed to transfer torsional loads from the wing to the center section as well as secure the wing laterally to negate any slop in the joint. Clamping sockets are bolted to the wing and fuselage structure and a pin is used to join the two pieces. The pin is clamped into place using two 4-40 hex head bolts that are inserted through small holes cut in the upper surface skin. Both the clamping sockets and the pins are designed to be constructed out of 2024 Aluminum and are secured to the airframe using 4-40 hex head bolts.

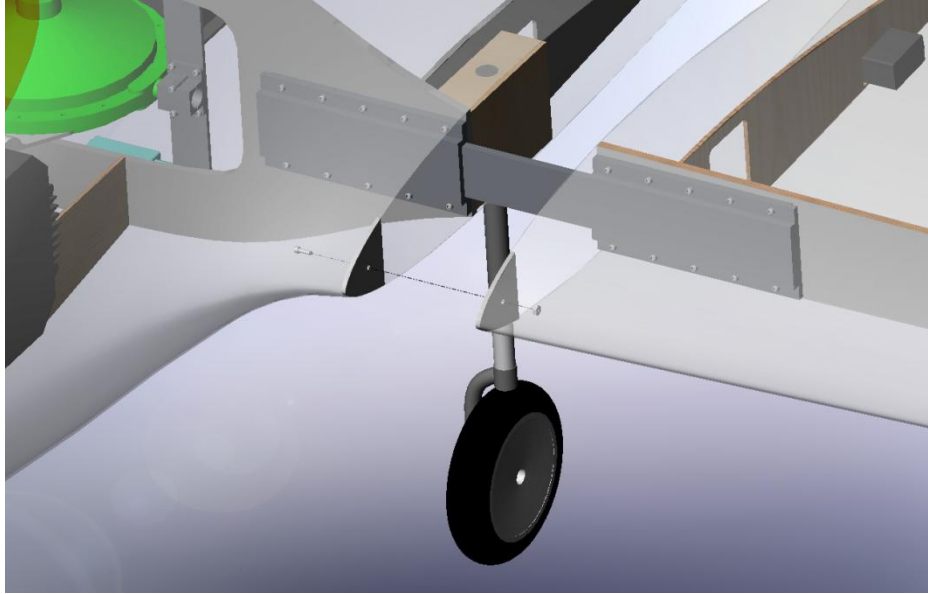


Figure 8: Wing-Fuselage Leading Edge Joiner Tabs

In order to provide additional lateral support to the wing-fuselage joint, tabs have been designed that are hard mounted to the leading edge of the joint profile for both the fuselage and the wing. These tabs will be made out of 1/8 inch birch plywood with a clearance hole for a 4-40 hex head bolt. Securing the bolt will provide a tight seam between the wing and fuselage and act to mitigate any remaining slop in the joint.

2.4 Empennage

The empennage of the aircraft has been designed with re-configurability in mind. The customer has specified that the aircraft have three different tail configurations: an aft tail configuration with desirable handling qualities, a true flying wing configuration with no tail, and an intermediate tail position. These three positions will allow for a progressive test plan where the operator can tailor the aircraft configuration for the desired operating state of the momentum wheel.

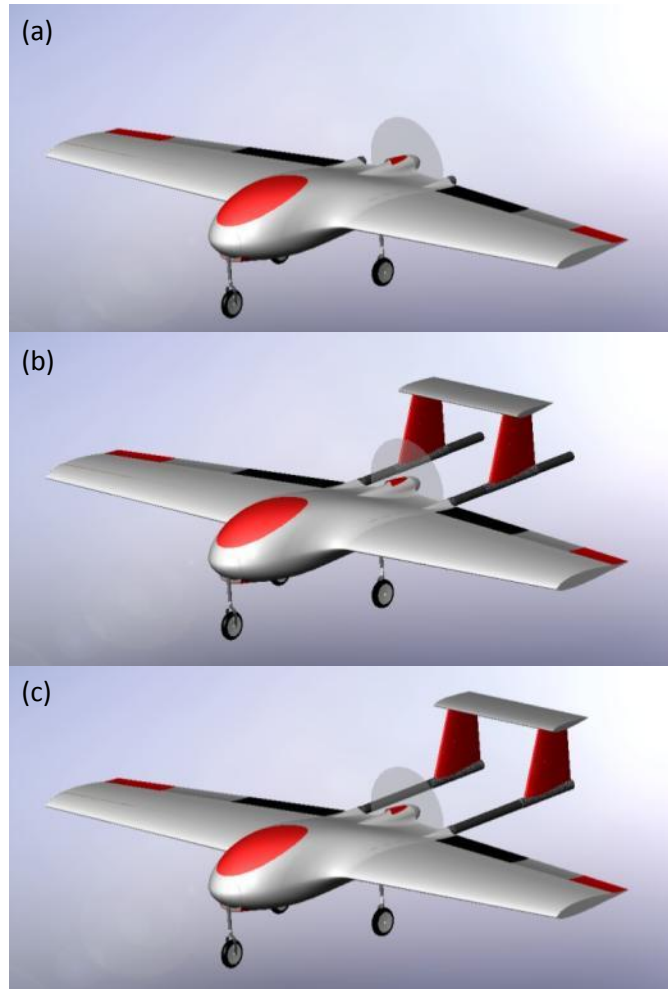


Figure 9: Tail Configurations: (a) Flying Wing Configuration, (b) Intermediate Tail Configuration, (c) Aft Tail Configuration

An additional tail configuration has also been designed into the aircraft. The horizontal tail is designed to be removable such that the empennage consists solely of the two vertical tails. This configuration affords a directionally stable platform without significantly affecting the pitch characteristics of the aircraft. This configuration will behave longitudinally like the flying wing configuration while reducing the risk of loss of directional stability during initial flight testing.



Figure 10: Vertical Tail Configuration

2.5 Momentum Wheel Mounting

The momentum wheel must be mounted such that there is sufficient strength in the mount and surrounding structure to transfer loads to and from the wheel. It is important that any flexure in the surrounding structure be reduced such that the wheel experiences only the actual angular rates and accelerations of the aircraft.

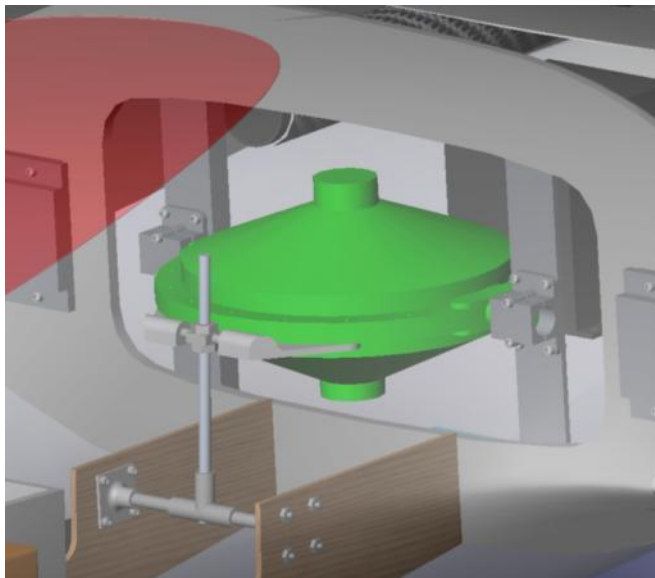


Figure 11: Momentum Wheel Mounting Configuration

Two pieces of aluminum angle are secured to back face of the main fuselage bulkhead to provide a strong and stiff mounting point for the momentum wheel. Clamping assemblies have been designed that bolt directly to the aluminum angle and secure the momentum wheel by its two spindles. The

clamping assemblies and aluminum angle are designed to support the moment wheel in translation as well as transfer rolling moments to and from the system. The clamps will provide some support about the pitch axis of the wheel through friction with the wheel spindles. In order to ensure that the wheel remains fixed in pitch, an additional assembly has been designed. Two boots bolt directly to the outer rim of the momentum wheel vacuum housing and support a spindle that is allowed to pivot freely. The spindle has a clearance hole for a #12-24 threaded rod that is secured to the spindle using two jam-nuts on either side. This threaded rod is connected to the fuselage longerons through a pivoting yoke assembly. This design will support the moment wheel in pitch and also allow the pitch angle of the momentum wheel relative to the aircraft to be set by the operator. To change the angle of the momentum wheel, the jam-nuts are loosened and the spindle is slid up or down the threaded rod to obtain the desired momentum wheel angle; the jam-nuts are then tightened to lock the wheel in place. This design offers +/- 15 degrees of continuous pitch rotation.

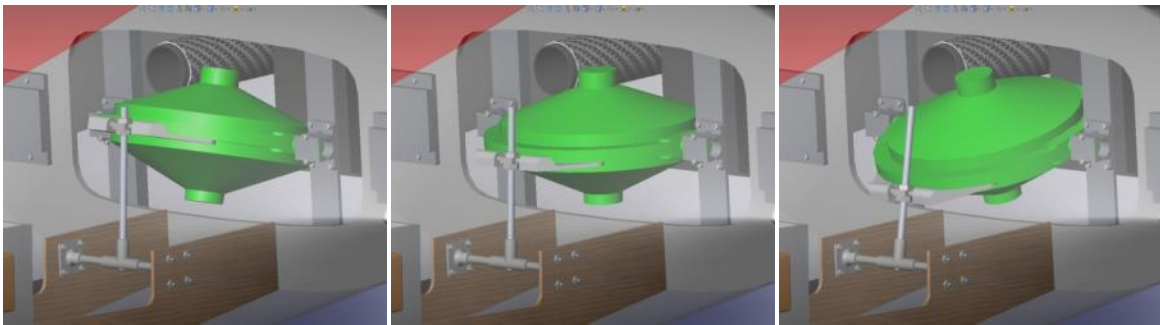


Figure 12: Momentum Wheel Pitch Angle Range: (a) +15°, (b) 0°, (c) -15°

2.6 Hatches

Accessibility has been an important part of the aircraft design. Providing easy access to all internal components will shorten the amount of maintenance time required and allow for efficient re-configurability and post-construction upgrades. It will also prove beneficial during pre-flight and post-flight inspections. A number of access hatches have been placed in locations where frequent and/or fast access to internal components is required.

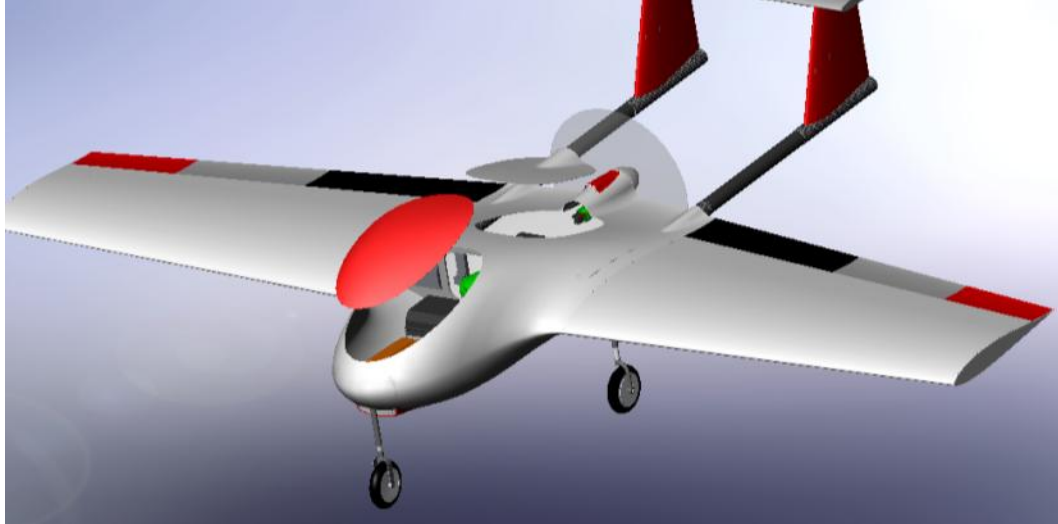


Figure 13: Fuselage Hatch Layout

The largest hatch is positioned at the nose of the aircraft where the majority of the internal components are located. This hatch will allow access to all of the flight batteries, flight computer, inertial measurement unit, receiver, power switches, and nose gear assembly. The front hatch will also provide access to the fuselage joiner socket assembly and leading edge joiner tab for wing attachment and removal. The second fuselage hatch is located aft of the main bulkhead and will provide access to the momentum wheel and all of its supporting components (battery, data recorder, and motor controller), propulsion motor and motor controller, and connection point for the tail booms.



Figure 14: Wing Hatch Layout

There are also two hatches located on the wings to provide access to the control surface servos. The first wing hatch is located on the lower surface approximately midway out on the wing. This hatch provides access to the middle control surface actuator and also helps with wire routing. The second wing hatch is located on the tip of the wing which provides access to the two actuators for the outboard control surface.

2.7 Landing Gear



Figure 15: Landing Gear Configuration

This aircraft is design to take off and land conventionally with tricycle landing gear. Robart 5/8" RoboStruts are rated for aircraft weighing up to 50 pounds and will be used for the landing gear; the offset struts will be used for the landing gear and the forked strut will be used for the nose gear. The main gear will also be outfitted with pneumatic disk brakes.

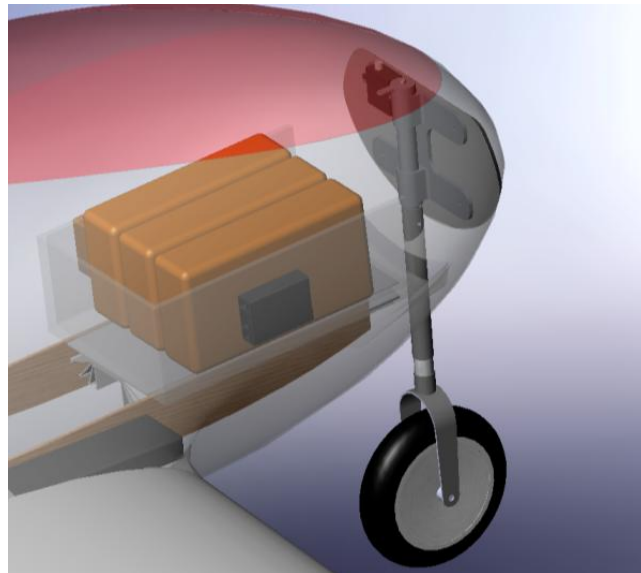


Figure 16: Nose Gear Mount

The nose gear is secured to the nose bulkhead by a butterfly style mount. This mount is designed to support the landing loads and the ground handling loads while allowing the nose gear to be steerable. The spindle of the nose gear mount has been designed to fail before the nose gear strut. The base of the spindle is necked down to a diameter that will cause the spindle to fail at that location for a load 4 percent lower than would normally break the strut. The spindle will be fabricated in house and is significantly less expensive and easier to replace than the strut. The butterfly mount also has mounting locations for the servo that will steer the nose wheel.

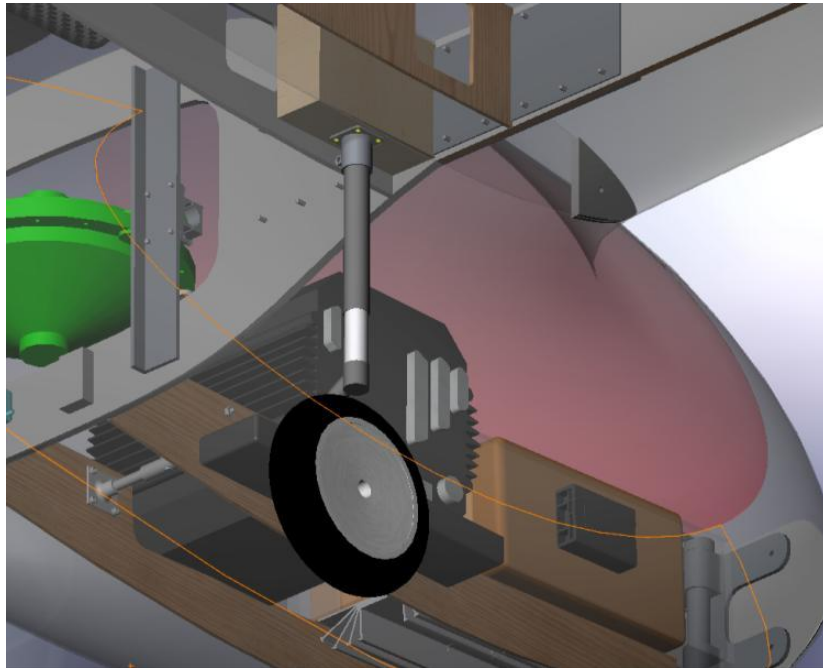


Figure 17: Main Gear Mount

The main gear are located on the outside face of the fuselage ribs slightly aft of the main fuselage bulkhead. The struts are inserted into a basswood block to support the gear vertically and in bending. The mounts that are included with the struts will be mounted to the bottom of the block and used to prevent the main gear struts from twisting and to hold the struts in the block. This mount assembly is designed to fail before the surrounding internal structure and is a much less critical part compared to the main fuselage bulkhead and fuselage ribs and is easily replaceable.

2.8 Mass Properties

The momentum wheel sizing and operational speed(s) will be largely determined by the moments of inertia of the aircraft. Thus, the moments and products of inertia for the flying wing configuration and the aft tail configuration are documented in the following table.

Table 1: Moments and Products of Inertia

	Without Tail	With Tail
I_{xx}	2.86 slug-ft ²	2.94 slug-ft ²
I_{yy}	1.14 slug-ft ²	2.43 slug-ft ²
I_{zz}	3.85 slug-ft ²	5.19 slug-ft ²
I_{xy}	0 slug-ft ²	0 slug-ft ²
I_{yz}	0 slug-ft ²	0 slug-ft ²
I_{xz}	0.0164 slug-ft ²	0.144 slug-ft ²

3. PROPULSION SYSTEM DESIGN

3.1 System Selection

Three types of propulsion systems were considered for use in this aircraft: a micro-turbine, a reciprocating engine, and an electric motor. The micro-turbine provides a low amount of system vibration leading to better data quality; however, it also requires supporting components and a large amount of fuel, both of which contribute to a relatively high overall system weight. Turbines also typically require a longer setup and engine start time which could reduce the amount of flight test time available. In contrast, a reciprocating engine based system has significantly lower weight and relatively short and simple flight preparation time. Reciprocating engines can produce a large amount of vibration which would lead to noisier data and a significant increase in fatigue loading on the momentum wheel mount and the surrounding airframe.

An electric motor based propulsion system affords a good balance between a turbine based system and a reciprocating engine based system. An electric motor system possesses the low vibration characteristics of a turbine engine while also having an overall system weight and ease of operation comparable to that of a reciprocating engine. Another beneficial attribute of an electric motor based system is that the system does not change weight throughout a given flight. This will allow for more accurate performance predictions as well as more accurate flight data due to the fact that the weight and center of gravity location will be known and remain constant throughout a given flight.

3.2 Motor selection

For initial motor selection it is desired that the system exhibit a power output to aircraft weight ratio of at least 50 watts per pound. This motor requirement is taken from the R/C community as a value appropriate for scale-like flight characteristics. A brushless motor configuration is also desired due to its comparatively higher operating efficiencies.

A commercial computer program, called MotoCalc 8, has been used to provide initial motor sizing and selection. MotoCalc is an electric propulsion system sizing and analysis tool used widely in the R/C community with a large database of performance data for electric motors, batteries, and speed

controls. A handful of candidate motors have been analyzed and compared to each other and to the derived propulsion system requirements. The motor selected for the aircraft through this process is the AXI 5330/18 brushless motor.



Figure 18: AXI 5330/18 Motor¹

Table 2: AXI 5330/18 Motor Specifications¹

Parameter	Value
K_v	259 RPM/V
Maximum Efficiency	90%
Maximum Efficiency Current	25-60 A (>85%)
No Load Current	2 A
Maximum Current	75 A / 60 s
Internal Resistance	32 mohm
Diameter x Length	2.48 in x 2.52 in
Weight	1.44 lb

3.3 Speed Control Selection

The speed control selected must be able to safely power the motor throughout its operating range; this includes adequate input voltage and current draw capacity. The speed control selected for the AXI 5330/18 motor is the Castle Creations Phoenix HV-110 Brushless Motor Controller.



Figure 19: Phoenix HV-110 Brushless Motor Controller²

Table 3: Phoenix HV-110 Speed Control Specifications²

Parameter	Value
Maximum Input Voltage	50 volts
Maximum Amp Draw	110 amps
Resistance	0.001 ohms
Length x Width x Height	2.8 in x 1.55 in x 1.25 in
Weight	0.33 lb

This speed control has a maximum input voltage of 50 volts and a maximum current draw of 110 amps both of which are larger than the required ratings of the motor (37 volts and 75 amps respectively). The speed control also has a ‘soft start’ capability to reduce the initial torque of the motor during spin-up preventing damage and fatigue to the surrounding airframe.

3.4 Battery Selection

The batteries for the propulsions system must provide the desired voltage (37 volts) and have a discharge rate appropriate for the chosen motor. The battery choice for this propulsions system is the FlightPower Evo F3A 10s pack.



Figure 20: FlightPower Evo F3A Battery

This battery pack has a capacity of 5000 mAh and a discharge rate of 25C; combining these two values results in a maximum discharge current of 125 amps, which will provide ample current to the motor along with a safety factor should the motor unintentionally draw more current than recommended.

As an initial requirement for the aircraft, it was determined that the propulsion system have enough capacity to sustain operation at full throttle for at least 10 minutes. The aircraft will not be operated at full throttle for this duration, this value is just used as a metric for propulsion system duration. It is estimated that an individual battery pack has enough capacity to provide 4 minutes of operation at full throttle. Thus, in order to achieve the necessary flight time, three of these battery packs will be arranged in parallel such that the resulting capacity of the system is 15,000 mAh which yields an estimated full throttle flight time of 12 minutes.

3.5 Propeller Selection

One of the major factors that have driven the propeller configuration is the distance between the tail booms. This space effectively limits the available diameter of the propeller. Thus, in order for the propeller to fit within the tail booms and still efficiently absorb the available power from the motor, a four-bladed propeller configuration is chosen. The four-blade design will effectively absorb the same amount of power as a larger diameter two-blade propeller. The resulting smaller propeller diameter will also contribute to the prevention of propeller strike during takeoff rotation and landing flare maneuvers. The propeller type chosen for the aircraft is a Zinger 4-Blade Pusher

propeller. The final diameter and pitch of the propeller is determined by the propulsion system testing and analysis to follow.



Figure 21: Zinger 4-Blade Pusher Propeller

3.6 System Configuration

The propulsion system configuration chosen for this aircraft is a pusher configuration with the motor and propeller located between the tail booms of the aircraft. The propulsion system components are highlighted in the following figure.

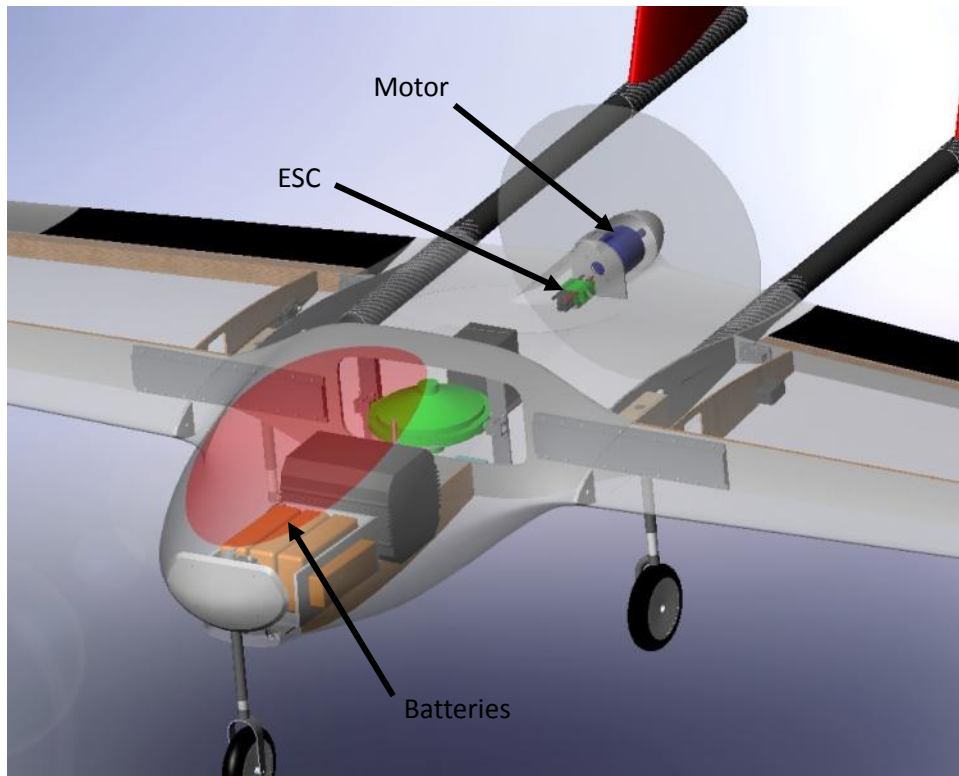


Figure 22: Propulsion System Layout

A component tray has been designed to secure the propulsion system batteries. Because the three propulsion system batteries comprise a substantial amount of mass relative to the other components, they are used to adjust the center of gravity for each flight configuration. The component tray is designed such that the batteries can be moved forward and aft to obtain the desired center of gravity. A spacer constructed out of blue foam is used to determine the longitudinal location of the batteries and to provide a bearing surface for the batteries when secured. Different spacers will be constructed to allow for simple adjustment of the aircraft center of gravity. The batteries are secured to the component tray using Velcro straps that travel over the top of each battery as well as around the front.

The tub portion of the component tray is constructed out of extruded aluminum u-channel to help transfer heat away from the batteries. Attached to the underside of the battery tray are three off-

the-shelf heat sinks which extend directly into the airflow provided by the cooling scoop allowing for more efficient heat transfer.

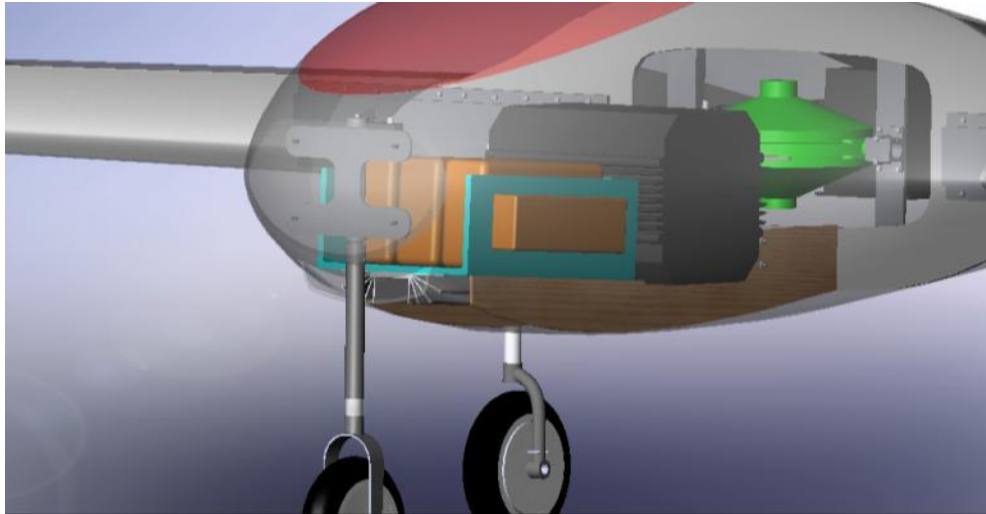


Figure 23: Battery Tray

The speed control is located in the aft section of the fuselage just forward of the motor bulkhead. By locating the speed control adjacent to the motor, only two wires are required to run the length of the airplane. If the speed control were located adjacent to the batteries, three wires are required to run the length of the aircraft increasing the complexity and the weight of the resulting wiring harness.

The motor is mounted to a dedicated bulkhead in the aft portion of the fuselage using M6 hex head bolts. On the motor side of the bulkhead, four standoffs are used to provide space between the back face of the motor and the bulkhead which will result in better motor cooling. To provide further cooling for the motor, a normal inlet is located on the top surface of the fuselage motor blend.

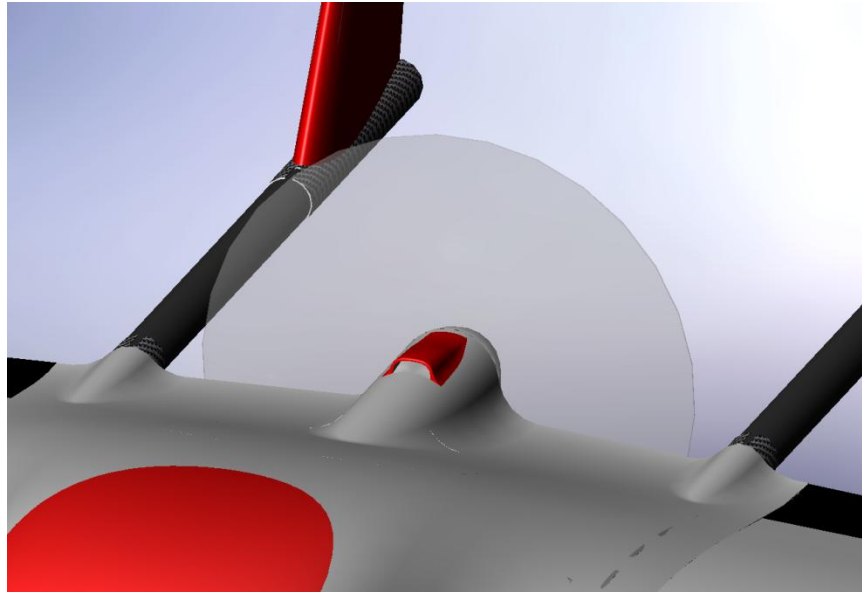


Figure 24: Motor Cooling Inlet

This normal inlet will direct airflow into the space between the motor and the bulkhead as well as around the motor can. The airflow will exit around the lower sides of the propeller spinner. The total pressure at the inlet of the duct and the negative pressure generated by the propeller at the exit will provide adequate cooling airflow through and around the motor in all flight conditions.

3.7 Propulsion System Wiring

The wiring harness layout for the propulsion system is illustrated below.

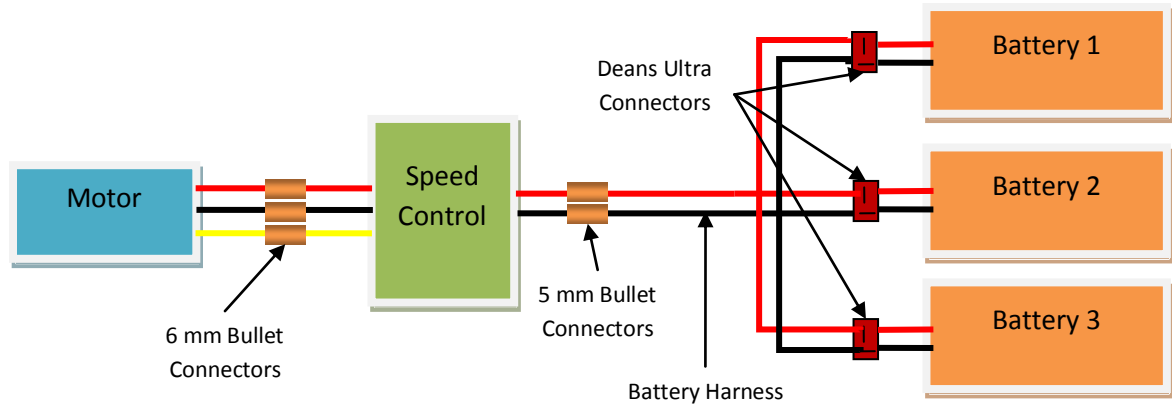


Figure 25: Propulsion System Wiring Harness Layout

Deans Wet Noodle 12-gauge wire will be used between the batteries and the speed control. A wiring harness has been fabricated to connect the three batteries in parallel. For ease of connection and disconnection, the battery connections will utilize Deans 2-Pin Ultra connectors which are rated to a max current draw of 50 amps. Because the batteries are connected in parallel, the current through these connectors is not expected to exceed the 50 amp limit. 5 mm bullet connectors (rated to 150 amps) will be used everywhere the current is expected to exceed 50 amps; namely the connection between the speed control and the battery. The speed control is manufactured with 10 gauge wire for the three leads that go to the motor; 6 mm bullet connectors will be used for this connection to better accommodate the larger wire.

4. PROPELLER TEST CELL DEVELOPMENT

The previous NCSU Subsonic Propeller Test Rig utilizes an under-slung motor and propeller assembly that is connected to the centerline sting by two beams. The thrust and torque generated by the motor and propeller are transferred to the sting through bending in the two beams. The beams are instrumented with strain gauges and the resulting strain of the beams is recorded and correlated to the thrust and torque of the motor/propeller assembly. This propeller balance could not be used for this application for two reasons. The beams are sized for a smaller motor/propeller combination and the thrust and torque generated by the propulsion system for this aircraft would likely damage the rig. Due to the offset thrust line, the larger propellers to be tested for this aircraft could be affected by the boundary layer of the tunnel floor or even come in contact with the tunnel floor.

To test the propulsion system for this aircraft in the NCSU Subsonic Wing Tunnel, a new propeller test cell (PTC) was designed. The PTC allows the motor and propeller to be mounted centerline in the wind tunnel, reducing the effects of the tunnel wall boundary layer, and is designed to withstand the predicted loads for the Plank propulsion system with a safety factor. The design requirements for the PTC were derived from the predicted motor performance, the desired resolution of the balance, and functionality. The maximum thrust and torque predicted by MotoCalc are 20 pounds and 2 ft-lbs. respectively. A safety factor of 2 was used to obtain the limit loads that the load cell must be able to withstand.

4.1 Configuration

A four arm, cruciform configuration was chosen for the PTC load cell.



Figure 26: PTC Load Cell

This configuration provides stability and support for the motor and propeller assembly reducing vibration during testing and adding durability for handling and assembling the balance. The four beam design transfers the thrust and torque loads of the motor-propeller assembly to bending in each beam which are measured using uniaxial strain gages. Thrust loads will result in tension and compression on the front and back faces of the beams and while subjecting the side faces of the beams to shear loading. Torque loads generate the reverse situation, the side faces of the beam are in tension and compression and the front and back faces in shear.

Uniaxial strain gages are used to measure the strain of the beams resulting from the thrust and torque loads. The strain gages are placed on all four faces of each beam and are aligned with the major axis of each beam, thus they predominately measure the deformation due to tension and compression loading and are relatively unaffected by deformation due to shear loading. This arrangement allows for two separate strain gage bridges to be formed: one predominately responsible for measuring thrust and the other for measuring torque. The thrust gages are located on the front and back faces of the beams and the torque gages are located on the side faces. Some

interactions between the two bridges was expected and is characterized and accounted for during calibration.

4.2 Material Selection

In selecting the load cell material, two requirements have been established: a low modulus of elasticity and a high yield strength. A material with a low modulus of elasticity will strain more under a given load than a material with a higher modulus of elasticity. The larger strain range allowed for a higher measurement resolution provided the maximum strain does not exceed the strain limit of the selected gages. A relatively high yield strength allows the material to withstand the necessary loads without plastically deforming. Material properties of candidate materials for the load cell are listed in the table below.

Table 4: Load Cell Candidate Material Properties³

Material	Modulus of Elasticity (ksi)	Yield Strength (ksi)	Ultimate Strength (ksi)
2024-T3 Aluminum	10,600	50.0	70.0
6061-T4 Aluminum	10,000	21.0	35.0
Titanium	16,800	20.3	31.9
260 Brass	16,000	10.9	43.5
302 Stainless Steel	28,000	37.0	84.8

The 2024-T3 Aluminum provides a good balance of low elastic modulus and high yield strength when compared to the other four candidate materials and was selected as the material for the load cell.

4.3 Load Cell Sizing

The overall diameter of the load cell is constrained by the size of the spinner used with the propeller. A 3.5 inch spinner was used for all candidate propellers, thus the diameter of the load cell is 3.5 inches to maintain a streamlined shape and reduce interactions with the propeller slipstream. The size of the load cell beams was chosen based on a number of factors. The beams must be large enough to withstand the necessary limit load conditions without plastically deforming but small enough to provide adequate measurement resolution. The minimum width of the beams is also

constrained by the size of the strain gages that are available. The entire gage and solder tabs must be able to fit on the faces of the beams in order to provide accurate measurements and ensure a proper bond. The cross-sectional dimensions chosen for the load cell beams are 0.1 inches wide and 0.1875 inches thick. The larger thickness dimension is due to the higher thrust loading, which requires a larger structural moment of inertia about that bending axis.

4.4 Load Cell Integration

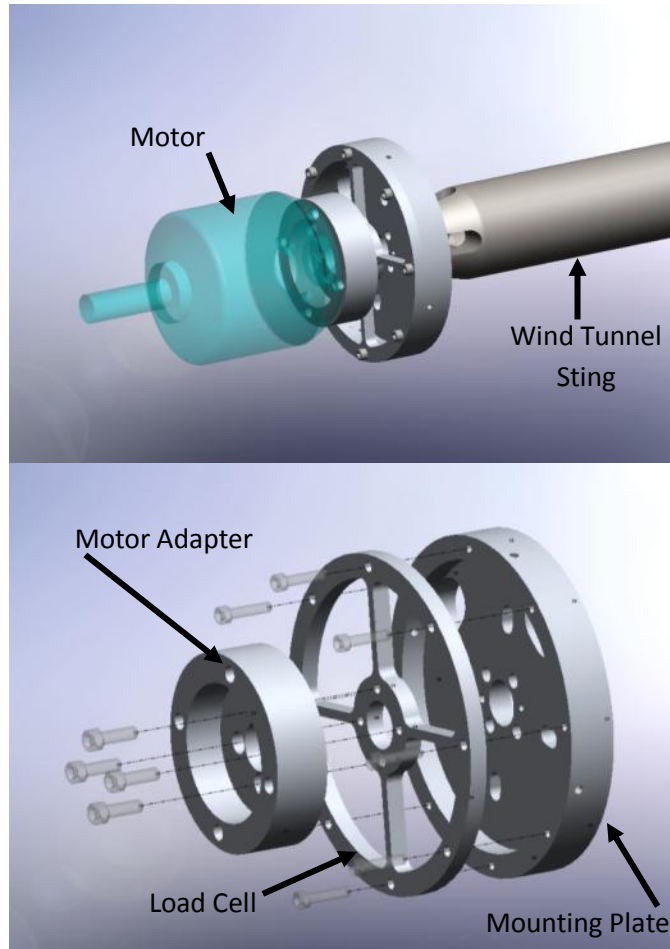


Figure 27: Propeller Test Cell Assembly

A three piece configuration was chosen for the propeller test cell structure which includes a motor adapter, load cell, and mounting plate. This configuration allows for future re-configurability in accommodating larger or smaller motors as well as a different sized load cell.

The motor adapter transfers the thrust and torque loads from the motor to the load cell and also acts as a thermal and electrical buffer between the two entities. The adapter was constructed out of acrylic which is non-conductive and thermally insulating. These two properties reduce the operating motor noise on the strain gage arrays as well as reduce conductive heating between the motor and load cell that could thermally load the beams and skew the measurement readings.

A mounting plate was designed to mount the assembly to the wind tunnel sting. This plate possesses sufficient strength to reduce the deformation under the expected loads which could affect the measurements. The mounting plate was constructed out of 6061 Aluminum which is lower cost compared to the 2024 used for the load cell while still maintaining sufficient strength. The plate has pass-through holes that allow access to the motor securing bolts and the motor, strain gage, and thermocouple wires.

4.5 ANSYS Analysis

A finite element model of the load cell assembly was constructed using ANSYS to help determine strain gage locations and provide an estimate of the expected strain under predicted load cases. All three components of the test cell (adapter, load cell, and mounting plate) are included in the model to best represent the actual load paths and constraints.

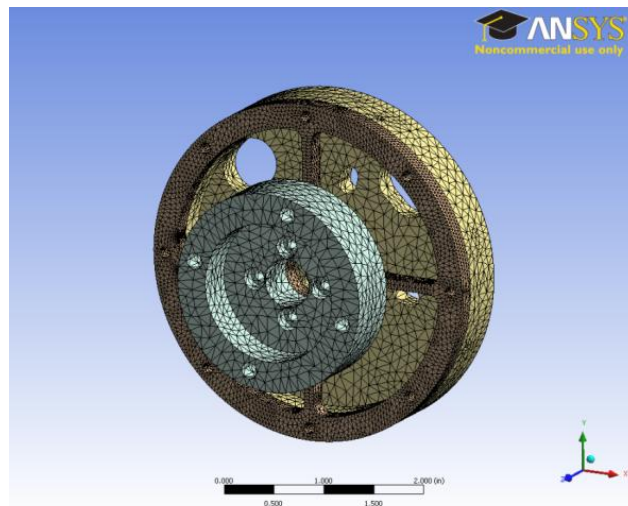


Figure 28: ANSYS Model of Propeller Test Cell Assembly

In the following figures the motor adapter and mounting plate have been hidden to show the load cell element more clearly. Three load cases were analyzed for both the design loads and the limit loads: pure thrust, pure torque, and both thrust and torque.

Table 5: Load Cell Design and Limit Load Values

Load Case	Design	Limit
Thrust	20 lbs	40 lbs
Torque	2 ft-lbs	4 ft-lbs

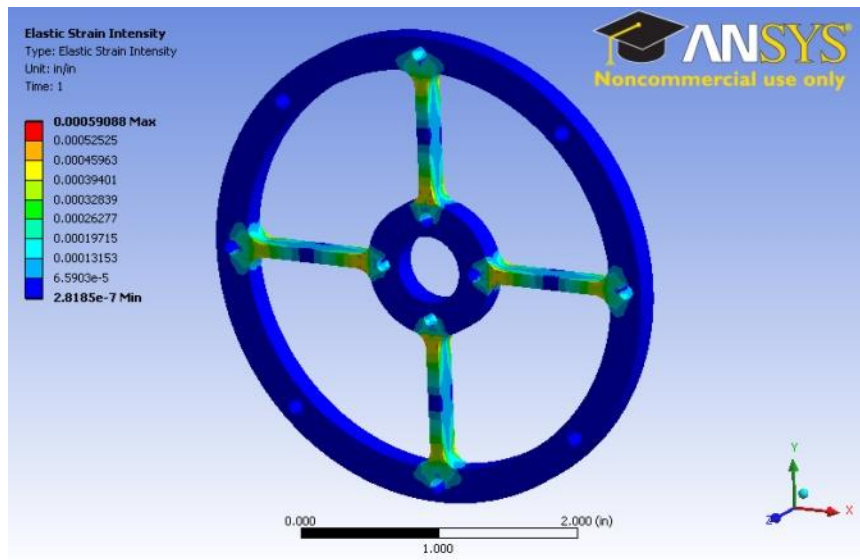


Figure 29: Strain Intensity Plot for Load Cell under Design Thrust Load (20 lbs)

Under a pure thrust load, the stress concentrates at both ends of each beam as a result of the cantilevered constraint at the hub and at the outer rim. At the hub, the front faces of the beams (as shown in the figure) are in tension while the back faces are in compression. The opposite is true at the outer ends of the beams. For the pure thrust case, the maximum strain (approximately 591 $\mu\epsilon$) occurs at the joint fillet between the beams and the center hub. A similar stress/strain distribution is observed for the pure thrust limit load case with a higher max strain of 1182 $\mu\epsilon$. Because the resulting strain is higher near the hub, the thrust specific stain gages were located on the front and back face of the beams near the hub of the load cell. Because the strain gages essentially average

the strain over the area of material covered by the strain gage grid, care was taken to ensure that the strain gages are not located in regions of large strain gradient. Thus the gages are placed as close to the hub as possible without overlapping the filleted portion of the beam.

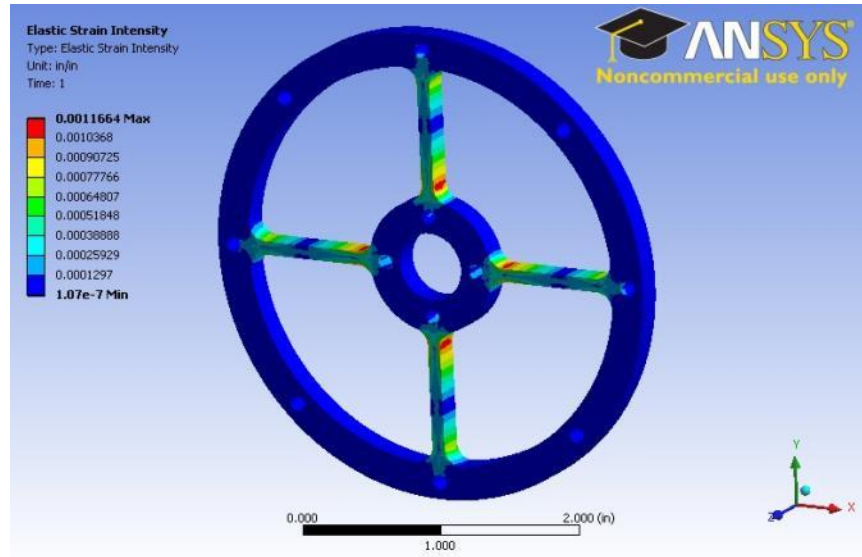


Figure 30: Strain Intensity Plot for Load Cell under Design Torque Load

For the pure torque case, a couple is applied to the motor adapter bolt holes. The torque load results in stress concentrations similar to the pure thrust case but on the sides of the beams. The maximum strain is again located on the beams at the fillet with the center hub and is approximately 1166 $\mu\epsilon$ in magnitude; 2333 $\mu\epsilon$ for the limit torque case. Thus, the torque specific gages will be placed on the sides of the beams near the hub again without overlapping the filleted region.

Although examining the pure thrust and pure torque cases provides insight into strain gage placement, the operational load cell will never be subjected to these specific load cases. During testing, the motor will be applying thrust and torque simultaneously. The following figure shows the strain distribution for the load cell under both design thrust and design torque.

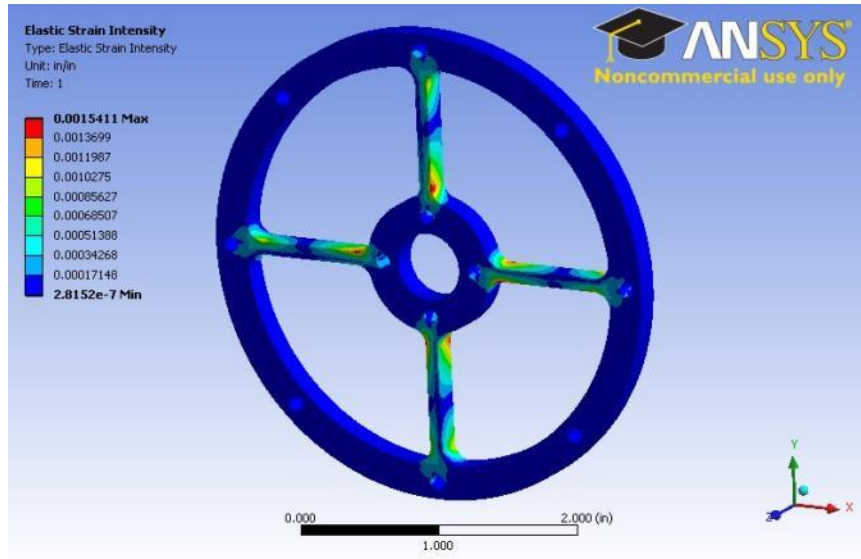


Figure 31: Strain Intensity Plot for Load Cell under Design Thrust Load and Design Torque Load

In the figure, the thrust is applied out of the page and the torque is applied in the counterclockwise direction. The maximum strain for this load case is +/- 1541 $\mu\epsilon$ and is located at the root of the beams in the opposite corners of the beam cross-section. Because the strain gages will essentially average the strain over the area covered by the gage grid, it is difficult to accurately predict the thrust and torque gage readings from this analysis. It was expected that some dependence between the thrust and torque measurements would exist. The magnitude of this dependence was determined during the load cell calibration process.

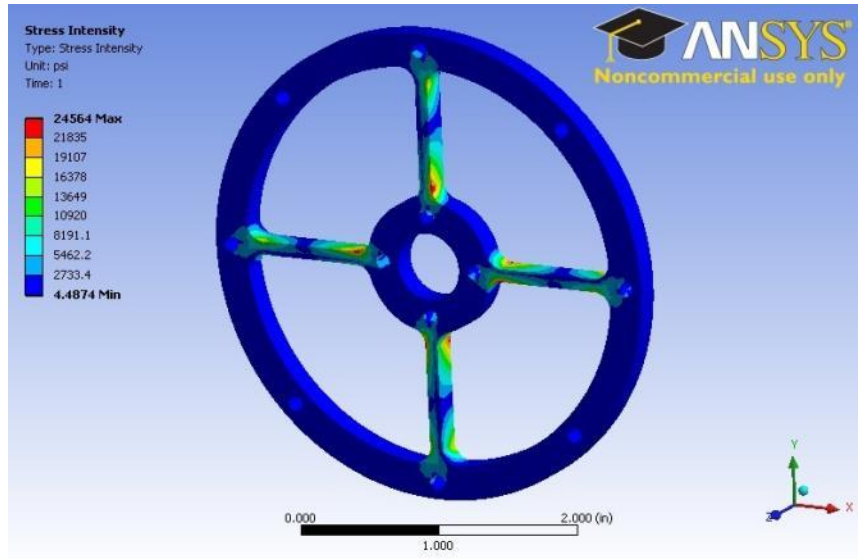


Figure 32: Stress Intensity Plot for Load Cell under Limit Thrust Load and Limit Torque Load

The simultaneous thrust and torque load case was also analyzed using the limit loads in order to ensure that the materials will not plastically deform. The maximum stress for the load cell under the limit load case is approximately 24,560 psi which is 49% of the yield stress for 2024 aluminum. The maximum stress in the motor adapter is approximately 1350 psi which is 13% of the yield strength of acrylic (10,700 psi)³. The maximum stress in the mounting plate under limit loads is 4414 psi which is 21% of the yield strength for 6061 aluminum.

4.6 Strain Gage Bridge Configuration

Two types of strain gages were chosen for the thrust and torque measurements. Due to the relatively small width of the front and back faces of the beams, the Vishay EA-13-031DE-350/E type strain gages were chosen for the thrust bridge. The gage matrix was trimmed such that the entire gage fits on the face of the beam while still providing a buffer between the edge of the gage matrix and the gage grid.

Table 6: Strain Gage Specs for Thrust Specific Gages (EA-13-031DE-350/E)⁴

Spec.	Value
Matrix Length	0.27 in.
Matrix Width	0.12 in.
Gage Length	0.14 in.
Grid Width	0.032 in.
Gage Factor	2.08 ± 1.0%
Resistance	350Ω ± 0.4%

Because the side faces of the beams are wider, a larger gage was selected for the torque bridge which has larger solder tabs resulting in a more simple installation. The type of gage used for the torque bridge is the Vishay EA-13-060LZ-120/E.

Table 7: Strain Gage Specs for Torque Specific Gages (EA-13-060LZ-120/E)⁵

Spec.	Value
Matrix Length	0.25 in
Matrix Width	0.15 in
Gage Length	0.16 in
Grid Width	0.09 in
Gage Factor	2.055± 0.5%
Resistance	120Ω ± 0.3%

The strain gage bridge type that was used for both the thrust bridge and torque bridge is a Wheatstone bridge with two active gages on each of the four arms. To better illustrate the layout of the two strain gage bridges, the following figure provides a number designation for each strain gage location. A 'Q' in the designation represents a torque gage and a 'T' in the designation represents a thrust gage.

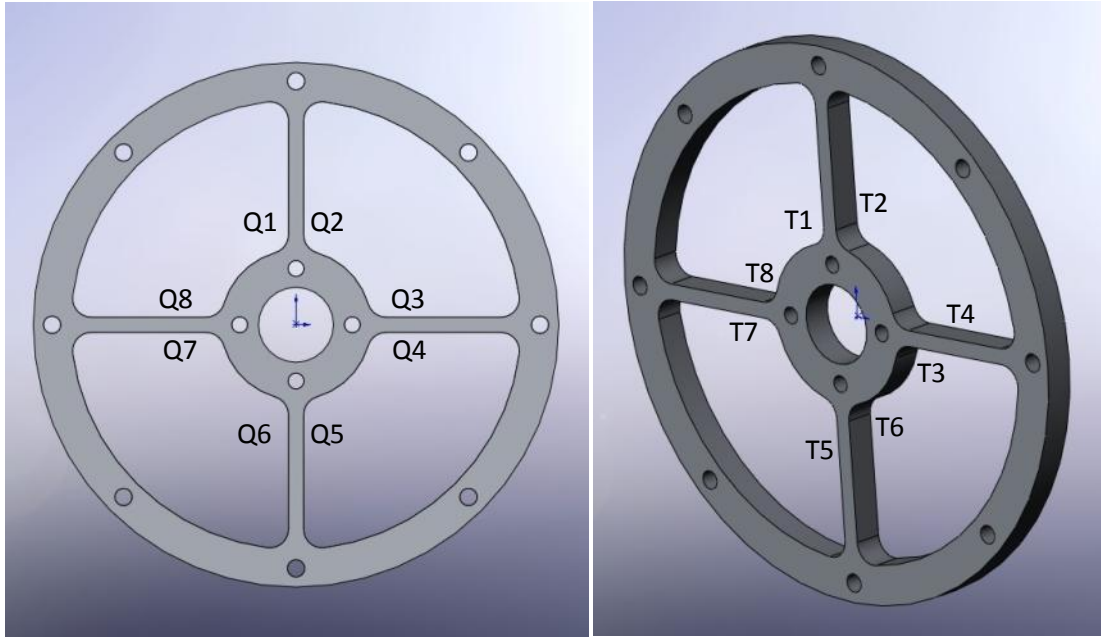


Figure 33: (a) Torque Gage Designation; (b) Thrust Gage Designation

The numbering for the torque gages begins with the left side of the top beam and proceeds around in a clockwise manner. The thrust gage numbering begins with the front face of the top beam and alternates front and back proceeding clockwise such that the odd numbers represent gages on the front face and even numbers represent gages on the back face. The thrust and torque bridge circuit diagrams are illustrated in the following two diagrams.

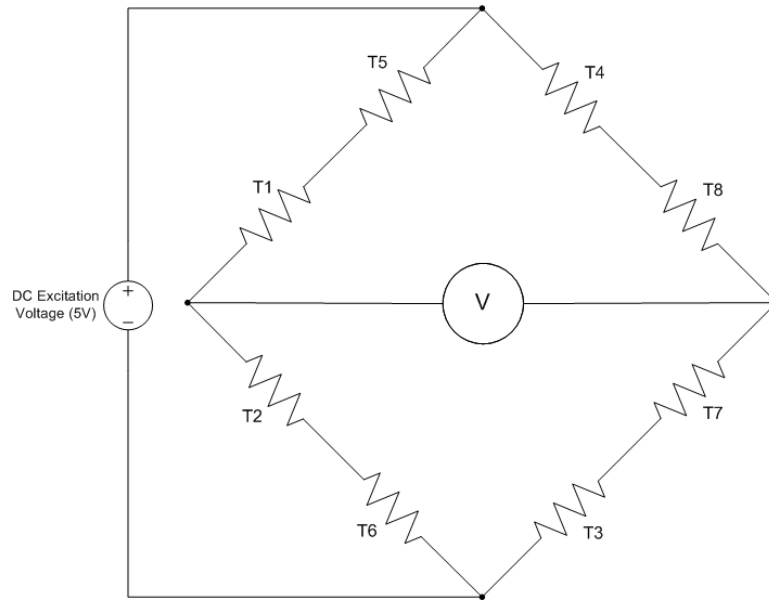


Figure 34: Thrust Bridge Circuit Diagram

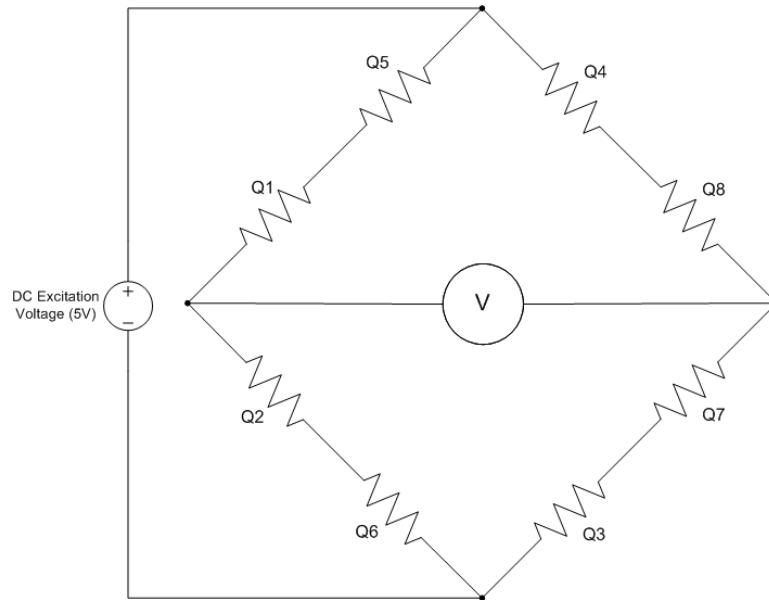


Figure 35: Torque Bridge Circuit Diagram

The output voltage from each bridge was measured independently using Vishay 2120 Strain Gage Conditioners and Power Supply. The Strain Gage Conditioners were connected to a National

Instruments A/D card and the output voltages of each bridge are recorded, converted, and displayed using LabView.

4.7 Constructed PTC

The different parts for the Propeller Test Cell were fabricated by the MAE Machine Shop. The strain gages are adhered in the pre-determined locations and connected in the appropriate bridge configuration outlined in Figures 34 and 35 using single conductor strain gage wire. These wires are secured, using epoxy, to the load cell and mounting plate to provide strain relief and prevent damage during handling. A shroud was constructed out of fiberglass to streamline the airflow around the balance and prevent aerodynamic loading and any adverse effects due to flow separation. Two holes were cut in the underside of the shroud to provide cooling flow for the motor.

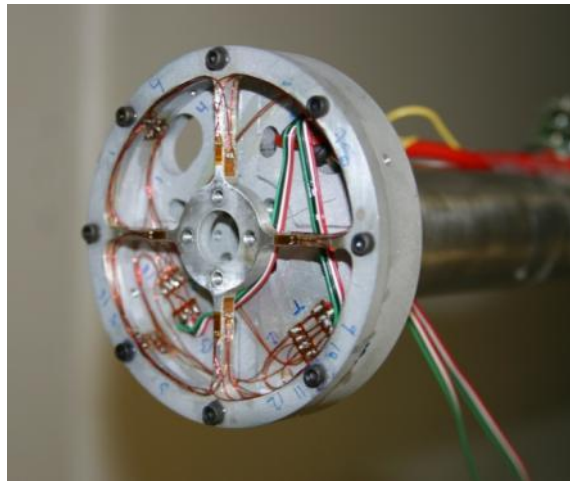


Figure 36: Propeller Test Cell with Motor Adapter Removed

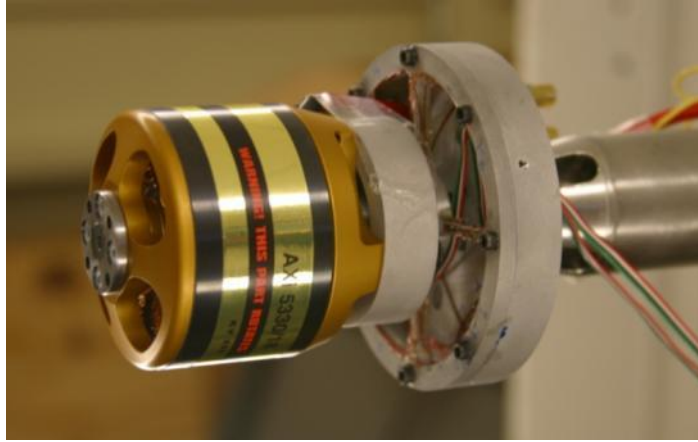


Figure 37: Propeller Test Cell with AXi 5330/18 Attached



Figure 38: Propeller Test Cell with Shroud Mounted on Wind Tunnel Sting

4.8 Calibration

With the balance constructed and installed on the wind tunnel sting, a calibration was performed to determine the calibration matrices that will be used to convert the output voltage of the strain gage bridges to thrust and torque readings. A randomized calibration run schedule has been generated using three equally spaced levels of thrust and torque that span the expected operating loads of the

PTC. The thrust loads that were used are 0, 15, and 30 pounds and the torque loads that were used are 0.5 foot-pounds and 1 foot-pound. Different motor assembly weights (0, 0.44, and 0.88 pounds) were also included in the calibration to ensure that the calibration values will not change with changing motor assemblies; different propellers or different motors. As a result, the randomized calibration run schedule (Appendix A) consists of multiple repetitions of each permutation of thrust, torque, and weight loadings.

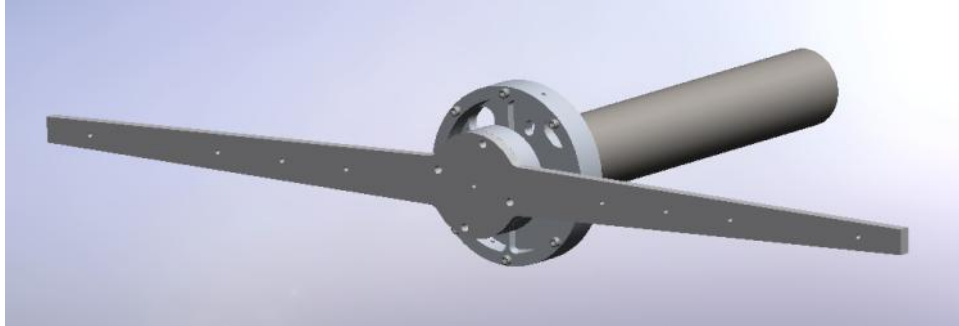


Figure 39: PTC with Calibration Bar attached

A calibration bar was designed in order to provide accurate and consistent weight locations for each calibration run. The calibration bar bolts to the motor adapter in the same manner as the motor. The bar has holes tapped for #4-40 bolts at radial stations of 0, 3, 4.5, 6, and 9 inches. Eye-bolts were screwed into these holes to provide two sets of equally spaced locations from which to hang weights. The hole drilled in the center of the calibration bar was used to apply the desired thrust loading and motor assembly weight.

The various permutations of thrust, torque, and weight were applied to the PTC based on the randomized run schedule and the resulting voltages were recorded. JMP statistical analysis software by SAS was used to analyze the calibration results and determine the calibration matrix and resulting model error. Full factorial model effects were applied to the three variables of pounds of thrust, foot-pounds of torque, and pounds of motor weight for modeling the thrust voltage and torque voltage.

In order to determine if each of the full factorial terms should be included in the model, the significance of each term has been estimated and analyzed. JMP evaluates the t-statistic and p-value of each model effect to assist in determining the significance of each term. A significance level of 0.05 was chosen in order to select the terms that will be incorporated in the final calibration model. A p-value of less than 0.05 (or a t-statistic with a magnitude greater than 2) indicates that the term is most likely a significant model effect. The following table displays the p-value and t-statistic for each term when applied to the Thrust Voltage model and the Torque Voltage model.

Table 8: Significance Indicators for Calibration Model Effects

Term	Thrust (V)		Torque (V)	
	t-statistic	p-value	t-statistic	p-value
Thrust (lb)	-3051	< 0.0001	17.07	< 0.0001
Torque (ft-lb)	-167	< 0.0001	1933.7	< 0.0001
Thrust (lb) * Torque(ft-lb)	0.58	0.5646	-0.09	0.9321
Weight (lb)	-2.67	0.0096	0.34	0.7375
Thrust (lb) * Weight (lb)	0.62	0.5406	0.27	0.7887
Torque (ft-lb) * Weight (lb)	-0.8	0.4289	-0.77	0.4442
Thrust (lb) * Torque (ft-lb) * Weight (lb)	-0.42	0.6734	-0.51	0.6129

For the Thrust Voltage model and the Torque Voltage model, pounds of thrust and foot-pounds of torque both produce a significant p-value of less than 0.0001. Each of the cross terms result in p-values much larger than 0.05 for both models and are regarded as insignificant. The weight term proves to be significant in the Thrust Voltage model with a p-value of 0.0096 and insignificant in the Torque Voltage model with a p-value of 0.7375.

To generate the calibration model, a Thrust (lb) model and a Torque (ft-lb) model was generated with Thrust Voltage, Torque Voltage, and Weight (lb) as model effects. In order to better determine the significance of motor assembly weight, the model uncertainty with and without weight as a model effect has been calculated.

Table 9: Calibration Model with Motor Assembly Weight

Term	Thrust (lb)		Torque (ft-lb)	
	Estimate	Standard Error	Estimate	Standard Error
Thrust (V)	-6.88	0.00221	0.00368	0.000212
Torque (V)	-0.372	0.00223	0.412	0.000213
Weight (lb)	-0.0293	0.0109	-0.000328	0.00104

Table 10: Calibration Model without Motor Assembly Weight

Term	Thrust (lb)		Torque (ft-lb)	
	Estimate	Standard Error	Estimate	Standard Error
Thrust (V)	-6.88	0.00212	0.00371	0.000193
Torque (V)	-0.374	0.00216	0.412	0.000197

The sensitivity estimates and standard errors in the above tables are used in coordination with the Kline-McClintock equation⁶ (Eq. 1) for estimating multi-variate uncertainty. Thrust and torque uncertainties were analyzed as functions of the thrust and torque bridge voltages and also with the additional variable of weight.

$$\delta y = \left[\left(\frac{\partial y}{\partial x_1} \delta x_1 \right)^2 + \left(\frac{\partial y}{\partial x_2} \delta x_2 \right)^2 + \left(\frac{\partial y}{\partial x_3} \delta x_3 \right)^2 + \dots \right]^{1/2} \quad [1]$$

where

$$y = f(x_1, x_2, x_3, \dots)$$

Table 11: Model Uncertainties with and without Motor Assembly Weight

Model	Uncertainty w/ Weight	Uncertainty w/o Weight
Thrust (lb)	± 0.0708 lb	± 0.0604 lb
Torque (ft-lb)	± 0.00647 ft-lb	± 0.00543 ft-lb

Notice that the model uncertainty increases with the addition of motor assembly weight as a model effect. Including weight introduces additional uncertainty into the model without increasing the

modeling confidence of the other two terms (Thrust Voltage and Torque Voltage) which results in a higher overall uncertainty. Thus, weight will not be included in the final calibration model.

The final calibration equation and matrix can be seen in Eq. 2.

$$\begin{pmatrix} Thrust(lb) \\ Torque(ft \cdot lb) \end{pmatrix} = \begin{bmatrix} -6.88 & -0.374 \\ 0.00371 & 0.412 \end{bmatrix} \begin{pmatrix} Thrust Voltage \\ Torque Voltage \end{pmatrix} \quad [2]$$

This model has a $\pm 0.2\%$ full scale accuracy for Thrust (lb) and a $\pm 0.3\%$ full scale accuracy for Torque (ft-lb). The model error is relatively small compared to other expected sources of error, such as mechanical noise from the rotating propeller assembly, and as a result is deemed negligible.

4.9 Signal Noise

During initial testing of the PTC, significant noise was observed on both the thrust bridge signal and torque bridge signal while the motor was running. Two common sources of noise were addressed; electromagnetic interference and structural vibration. Steps were taken to isolate the high current propulsion system power lines from the load cell signal lines to reduce any radio frequency interactions between the two groups of wires. The propulsion system power lines were also oriented orthogonal to the load cell signal lines to further reduce any interaction between the two circuits. However, neither of these actions produced any noticeable benefits.

The data collection system was changed to a Vishay System 6000, which can sample the strain gage bridges up to 10 KHz. This allowed for further examination of the noise characteristics. The StrainSmart software package was used for a Fast Fourier Transform (FFT) and power spectrum analysis of the strain gage signals for different motor RPM.



Figure 40: Power Spectrum Analysis of Motor RPM Progression through Resonance

The large spike in each plot corresponds to the motor RPM and is a result of the commutation frequency of the motor ($\frac{RPM}{60} * \frac{\# \text{ of poles}}{2}$). The rotation of the poles, commutation, is what provides torque to the motor, and this impulse at each rotation of the motor poles is being measured by the PTC load cell. As the motor RPM is increased and this pole rotation frequency approaches a frequency of approximately 325 Hz the amplitude begins to increase and peaks at a frequency of approximately 340 Hz before falling off as the motor RPM continues to increase. This sudden increase in amplitude is a result of resonance as the commutation frequency interacts with a structural mode of the PTC.

In order to verify that the commutation frequency was exciting a structural mode of the PTC, some tests were performed to identify the frequencies of the structural dynamics. The PTC structural dynamics were excited by applying a simulated impulse in both the thrust direction and about the torque axis. The StrainSmart power spectrum analysis was again used to analyze the signals from the thrust and torque bridges.

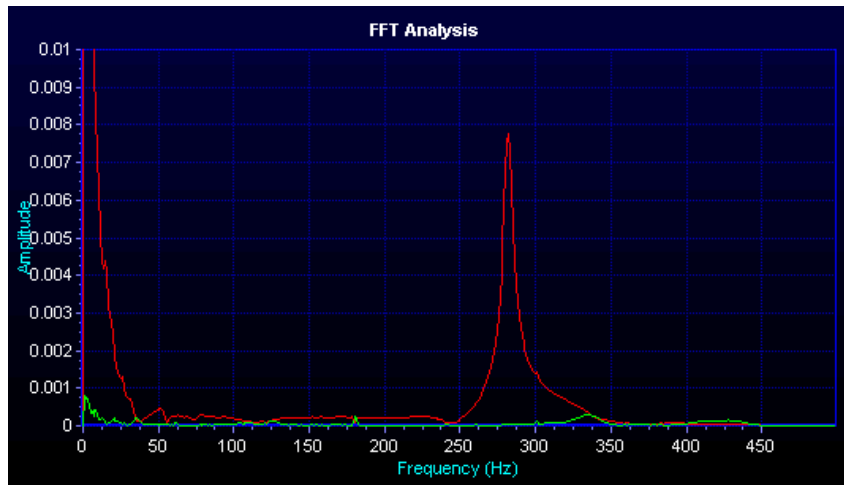


Figure 41: FFT Analysis for Thrust Impulse on PTC

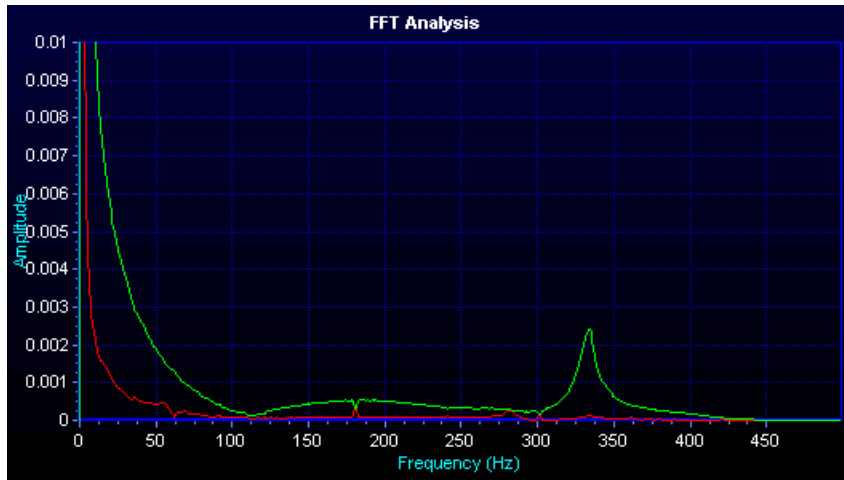


Figure 42: FFT Analysis for Torque Impulse on PTC

The thrust impulse excited a mode at approximately 280 Hz while the torque impulse excited a mode at 340 Hz. The natural frequency of the PTC in the thrust direction has been calculated to further confirm the frequency of this structural mode. ANSYS was used to determine the spring constant of the load cell. For 20 pounds of force in the thrust direction, the load cell deflected approximately 0.00105 inches resulting in a spring constant of 228000 lb/ft. The undamped natural frequency of the PTC was then calculated using the following equation.

$$\omega_n = \sqrt{\frac{k}{m}} \quad [3]$$

Using the motor adapter, motor, and propeller adapter as the mass of the system, the natural frequency was calculated to be 2140 rad/s or 341 Hz. This frequency is slightly higher than the frequency observed in Figure 41. However, the frequency measured in the power spectrum analysis is the damped natural frequency which is lower than the undamped natural frequency.

Because the motor commutation frequency introduces a significant amount of noise into the measurements, a 5 Hz, 5th order Butterworth filter has been applied in LabVIEW to reduce this high frequency noise. This filter will also filter out noise due to imbalance of the propeller assembly which can be seen as the small peak in the 50 Hz range of Figure 40. The operator must be diligent to avoid sustained operation of the motor at an RPM that results in a commutation frequency near

the resonance frequency of either structural mode (approximately 2600 to 3000 RPM or integer multiple thereof) during testing as this could result in damage to the load cell.

5. WIND TUNNEL TESTING:

5.1 Equipment

The propulsion system and three different propellers were tested in the NCSU Subsonic Wind Tunnel. This tunnel is a close circuit tunnel with a 32 inch by 45 inch test section capable of reaching speeds in excess 100 ft/s. The PTC was mounted on the centerline sting in the tunnel.



Figure 43: Medusa Power Analyzer Pro

A Medusa Research Inc. Power Analyzer Pro was chosen to record the real-time operating conditions of the electrical propulsion system during wind tunnel testing. The unit is connected inline between the batteries and the electronic speed control ESC. The Power Analyzer is capable of recording current, voltage, power, amp-hours consumed, watt-hours consumed, motor RPM, and two different temperatures; each of these values were recorded continuously during testing at a sampling rate of 4Hz. Only one of the thermocouples was used during the tests to record motor temperature. This unit was connected to the receiver input on the speed control and used to control the motor during testing. The unit allows for manual control of the motor as well as the use of preprogrammed, user defined throttle sequences. The Power Analyzer communicates via USB link to a laptop. The PowerPROview software provides a user interface to control the motor from a GUI on the laptop computer. This program allows the data to be monitored and recorded on the laptop for later analysis.

Vishay 2120 Strain Gage Conditioners and Power Supply are used to supply both bridges with the proper excitation voltage and condition the signal from each bridge. The conditioners allow the user to zero the signal as well as apply a gain to the signal. The conditioners are used to zero the signal from the strain gage bridges prior to each test run. The gains for the two bridges are set during calibration to yield 4.5 volts for the full scale load values. The signal is sent from the conditioners to a National Instruments A/D card that is monitored using LabVIEW. A LabVIEW program has been written that records, processes, displays, and saves the data from the strain gage bridges along with the atmospheric and tunnel conditions.

5.2 Experiment Procedure:

The propellers are tested in the wind tunnel over a range of advance ratios (J).

$$J = \frac{V}{n d} \quad [4]$$

Advance ratio varies with tunnel velocity and RPM for a given propeller. For a given test series, the throttle position remains constant and is set such that the motor is operating safely away from the resonance frequencies of the PTC. The tunnel velocity is then varied in 5 ft/s increments starting at approximately 20 ft/s and ending when the propeller is no longer producing thrust. The propeller RPM will vary with changing inflow conditions and is monitored to ensure the system does not approach resonance conditions. At each data point, the system is allowed to reach equilibrium and the tunnel conditions and thrust and torque loads are recorded using LabVIEW. The motor data (RPM, current, voltage, and temperature) is recorded continuously throughout the run using the Power Analyzer.

5.3 Data Reduction

5.3.1 Temperature Correction:

While performing initial testing with the propulsion system and the PTC, a residual thrust reading was observed following a given run after the system had been powered down. It has since been determined that this residual thrust is due to temperature effects on the load cell. The motor generates a significant amount of heat which acts to warm the air inside of the PTC shroud. The temperature of the air inside of the closed circuit wind tunnel also increases. Both of these factors contribute to thermally load the load cell. In order to adjust the thrust data for these temperature effects a time based linear correction was determined.

$$T_{corr} = T_{reading} - T_{residual} \left(\frac{t}{t_{total}} \right) \quad [5]$$

Thus, as the motor and load cell heats up during testing, an increasing larger percentage of the residual thrust reading is subtracted from the current reading.

5.3.2 Blockage Correction

The propeller disk area is not insignificant when compared to the test section cross-sectional area (16% of the tunnel area for a 17 inch prop), thus a correction must be made to the propeller inflow velocity. A propeller producing thrust accelerates the airflow passing through it resulting in a slipstream with a higher velocity compared to the tunnel velocity. However, because the airflow is constrained by the tunnel walls, the volume of air passing through the propeller must equal the volume of air passing aft of the propeller. This results in a local velocity outside of the propeller slipstream lower than the tunnel velocity and a higher static pressure in the region behind the propeller. This higher pressure produces an additional force on the propeller in the thrust direction as if it were operating at a lower freestream velocity.

A number of correction methods exist to account for these effects on the propeller. Fitzgerald⁷ has analyzed the accuracy of three prominent correction methods: Glauert, Hackett-Wilsden, and Sørensen and Mikkelsen. Fitzgerald has shown that the Glauert correction provides equal or better accuracy compared to the other correction methods over the range of thrust coefficients

experienced in this testing. The Glauert correction does not require any additional pressure measurements or instrumentation. Due to its simple implementation and proven accuracy, the Glauert correction⁸ has been chosen for this research.

$$\frac{V'}{V} = 1 - \frac{\tau \cdot \alpha}{2\sqrt{1 + 2\tau}} \quad [6]$$

$$\tau = \frac{T}{(\rho AV^2)} \quad \alpha = \frac{A}{C}$$

T = thrust (lb)

ρ = density (slug/ft³)

A = propeller disk area (ft²)

C = wind tunnel cross-sectional area (ft²)

V = wind tunnel velocity (ft/s)

V' = corrected velocity (ft/s)

The corrected velocity is determined by multiplying the ratio determined in Eq. 6 by the measured tunnel velocity.

5.4 Results

5.4.1 Propeller Data:

The thrust and power produced by each propeller tested have been non-dimensionalized using the following coefficients⁸. The results are presented in Figures 44 and 45.

$$c_T = \frac{T}{\rho n^2 d^4} \quad [7]$$

$$c_P = \frac{P}{\rho n^3 d^5} \quad [8]$$

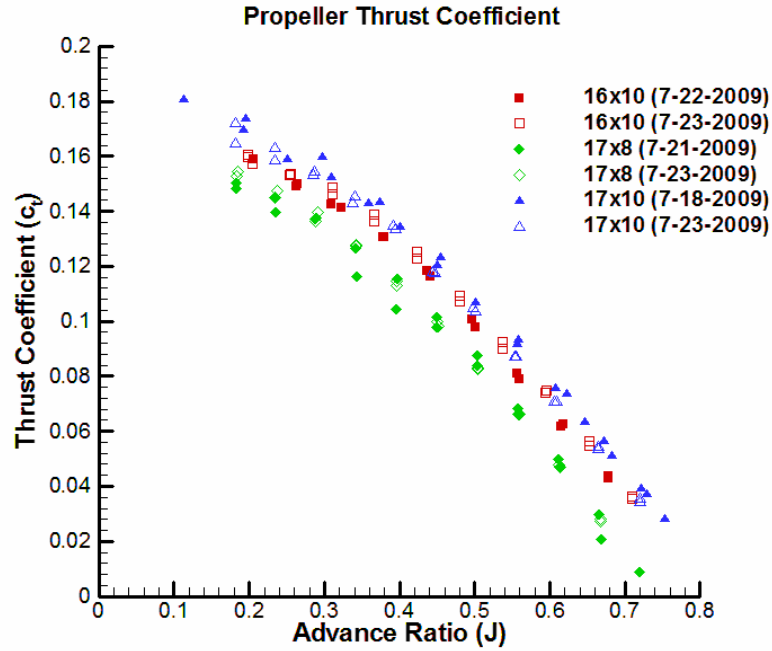


Figure 44: Propeller Thrust Coefficient

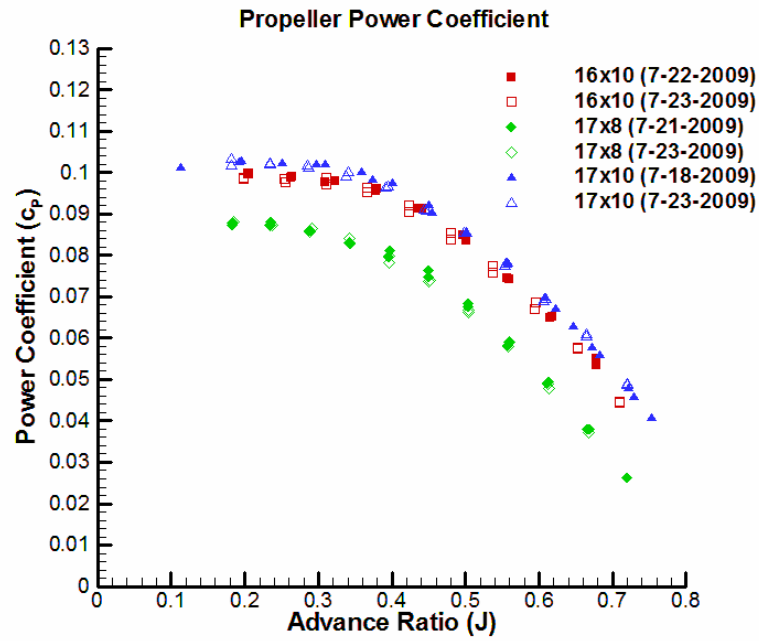


Figure 45: Propeller Power Coefficient

The 17x8 propeller produces lower thrust and power at a given advance ratio due to its lower pitch, which indicates that this propeller will operate at a higher RPM for a given flight speed and motor power than the other two propellers. The 17x10 produces slightly higher thrust and absorbs slightly higher power than the 16x10 due to its larger diameter.

The propeller efficiencies have also been calculated.

$$\eta = \frac{TV}{Q\Omega} \quad [9]$$

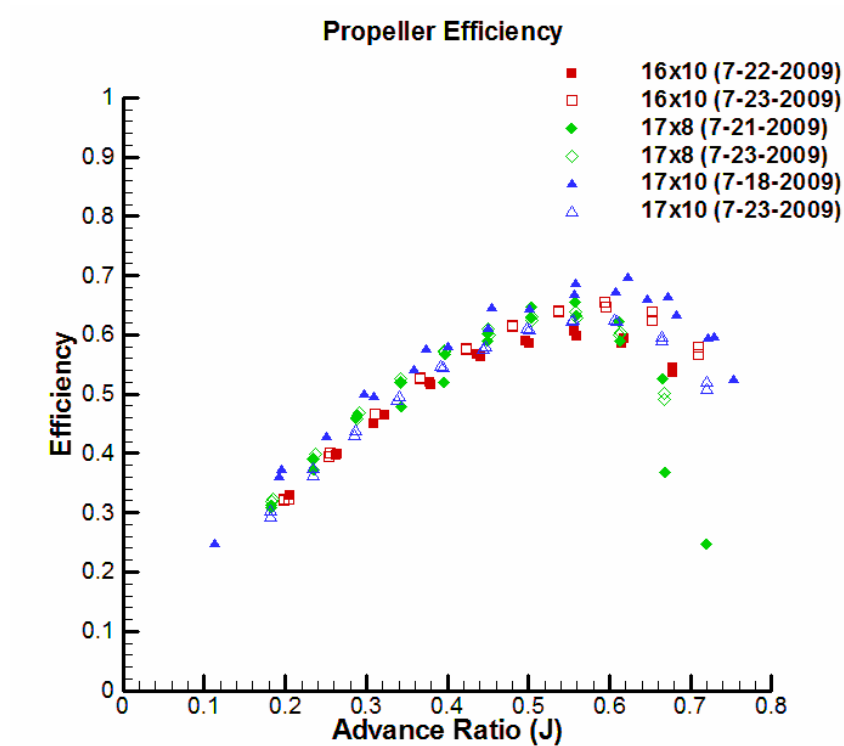


Figure 46: Propeller Efficiency

The efficiency curves for the 17x10 and 16x10 propellers are very similar in shape with the 17x10 having a slightly higher efficiency for a given advance ratio. The 17x8 propeller has approximately equal efficiency to the 17x10 at lower advance ratios but peaks sooner than both the 17x10 and 16x10 props. The peak efficiency for the 17x10 propeller (~65%) and the 16x10 propeller (~67%) occurs at an advance ratio of approximately 0.6 while the peak efficiency of the 17x8 propeller

(~66%) occurs at the lower advance ratio of 0.55 which is expected due to the lower pitch of the later propeller.

The speed-power coefficient has also been calculated for each propeller. This coefficient is typically used in determining optimum propeller diameter⁹. However, a larger propeller performance sampling for different diameters and pitches is suggested for this approach, and for this research the aircraft performance under each propeller is calculated directly reducing the need for alternate methods of propeller diameter selection.

$$c_s = \sqrt[5]{\frac{\rho V^5}{P n^2}} \tag{10}$$

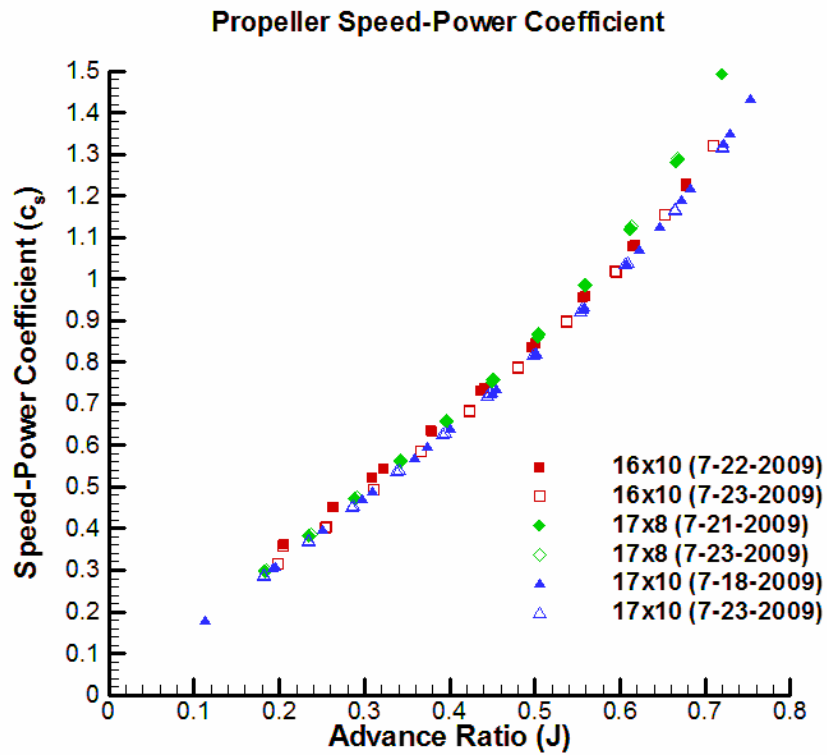


Figure 47: Propeller Speed-Power Coefficient

5.4.2 Thrust and Power Available:

The Initial plan was to obtain thrust and power available data by wind tunnel testing the propulsion system up to full throttle. However, temperature and vibration issues arose resulting in testing being cut short in fear of damaging the motor, speed control, and/or balance. In order to obtain an estimate of thrust and power available, propeller data at lower throttle settings and dc motor theory will be used concurrently.

According to dc motor theory, motor torque is a function of current.

$$Q_m = \frac{(i - i_0)}{K_Q} \quad [11]$$

The torque coefficient and no load current are constant for a given motor. The torque coefficient is assumed to be equal to the speed coefficient (K_V) in the units of amps/lb-ft.¹⁰ For this application, the motor current at full throttle is assumed to be constant resulting in constant torque. This assumption is made on the basis of how the motor will be operated. Should full throttle result in a current draw larger than the maximum continuous current of the motor, the throttle setting will be reduced in order to prevent damage to the motor. Thus, the full throttle current draw will, in effect, be regulated to the maximum continuous current draw of the motor: 75 amps. The resulting torque value determined from Eq. 11 is 1.99 ft-lb.

This torque value and constant torque trend are also reflected in the MotoCalc analysis. The torque estimated by MotoCalc is relatively constant, varying between approximately 1.87 and 2.01 ft-lb over the majority of operating conditions until the propeller begins to overspeed and unload the motor. The full throttle wind tunnel data recorded prior to prematurely stopping the test also supports this constant torque assumption with values centered around 2 ft-lb.

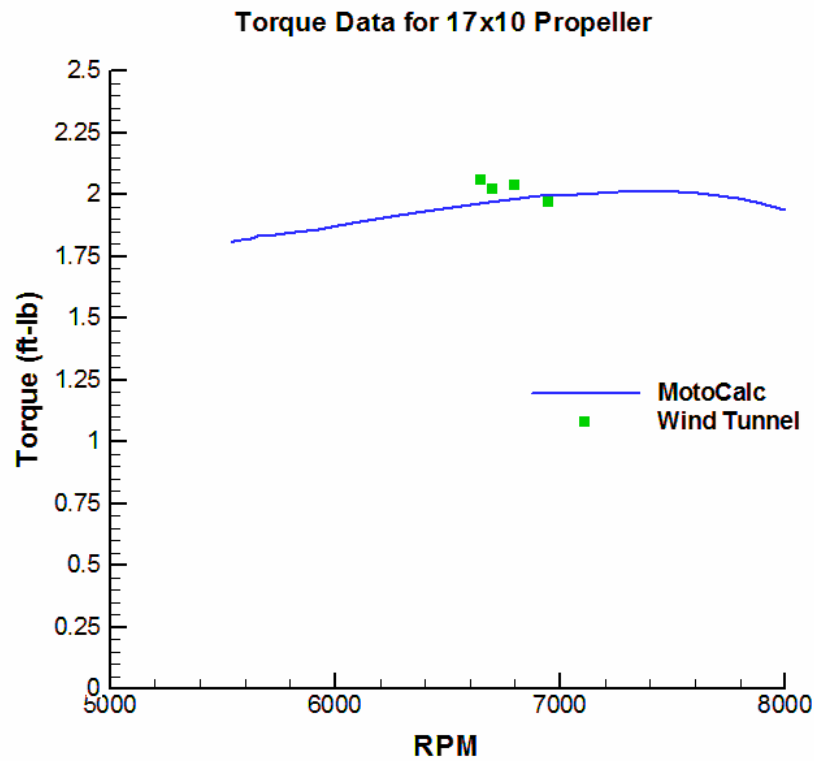


Figure 48: Torque for 17x10 Propeller

To calculate the resulting thrust and power available from the propulsion system, an iterative method was used to determine the equilibrium RPM at which the power produced by the motor is equal to the power being absorbed by the propeller. The power produced by the motor is calculated using the following equation.

$$P_m = Q \cdot \Omega \quad [12]$$

The power absorbed by the propeller is obtained by applying a second order polynomial fit to the propeller power coefficient (Figure 45); the resulting equations are a function of advance ratio.

$$\begin{aligned} c_{P,17x10} &= (-0.217)J^2 + (0.095)J + 0.092 \\ c_{P,16x10} &= (-0.251)J^2 + (0.123)J + 0.084 \\ c_{P,17x8} &= (-0.240)J^2 - (0.101)J + 0.077 \end{aligned} \quad [13]$$

The power absorbed by the propeller is then calculated using the power coefficient and equated to the power output of the motor and solved for RPM. This equilibrium RPM is then used to calculate the thrust available at the respective airspeed using a linear curve fit on the thrust coefficient of the propeller.

$$\begin{aligned}
 c_{T,17 \times 10} &= (-0.211)J^2 - (0.058)J + 0.189 \\
 c_{T,16 \times 10} &= (-0.266)J^2 - (0.008)J + 0.172 \\
 c_{T,17 \times 8} &= (-0.274)J^2 - (0.022)J + 0.165
 \end{aligned}
 \tag{14}$$

The thrust is then multiplied by the respective airspeed to obtain the power available. The thrust available and power available are displayed in the following figures for each of the three propellers tested.

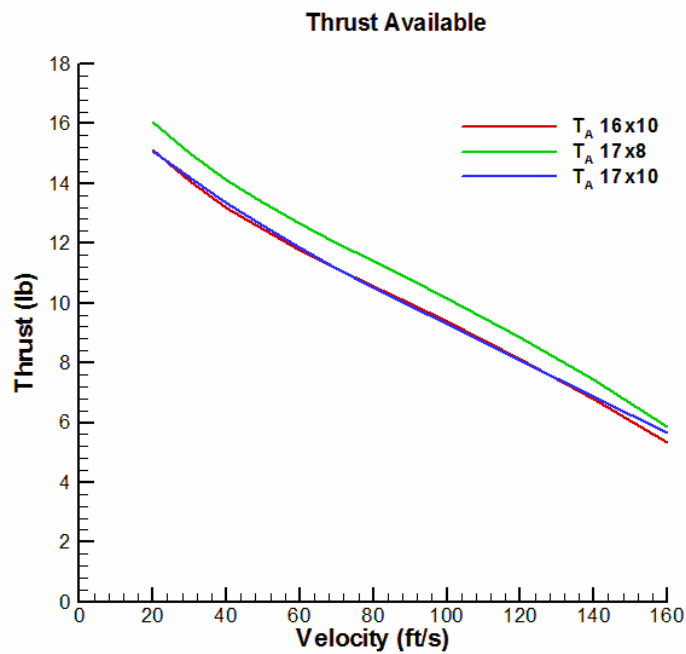


Figure 49: Thrust Available

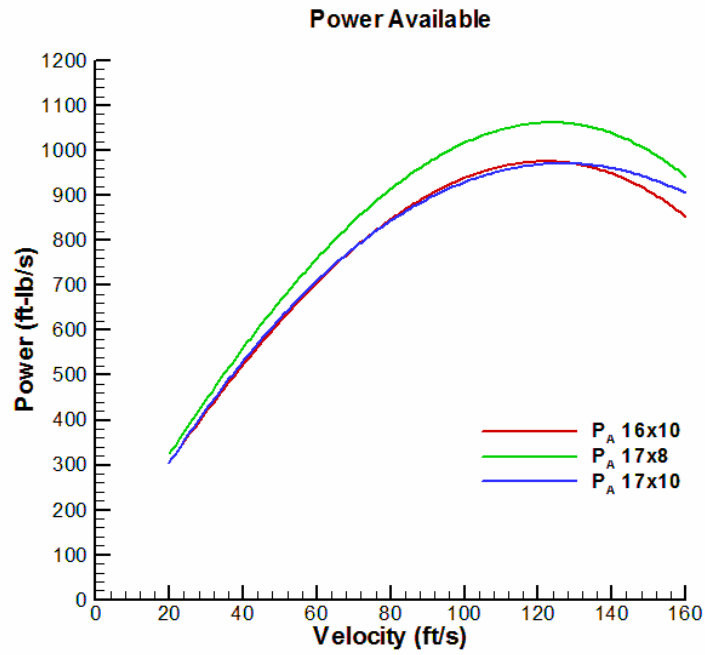


Figure 50: Power Available

6. AIRCRAFT PERFORMANCE ANALYSIS

To determine which of the three tested propellers provides the best fit with the remainder of the propulsion system and the aircraft, several propulsion system dependent performance aspects have been evaluated for each tested propeller. These parameters include maximum steady level speed, range, endurance, rate of climb, and takeoff performance.

6.1 Parasite Drag Estimation

To perform the performance analysis of the aircraft an estimate of parasite (viscous) drag is required to fully characterize the aerodynamics. To estimate the parasite drag of the aircraft, a component buildup technique outlined by Raymer¹¹ is used. This method relates flat-plate skin friction drag to the different components of the aircraft using a component 'form factor' which provides an estimate of the drag due to viscous separation. Below is a table of the parasite drag generated by each individual component.

Table 12: Component Parasite Drag Contributions

Component	$C_{D0,c}$
Wings	0.0078
Verticals	0.0010
Horizontal	0.0011
Fuselage	0.0055
Booms	0.00055
Landing Gear	0.0015
L & P	0.0035

The term 'L & P' stands for leakage and protuberance which accounts for the drag generated by exposed servo horns and control rods, hatches that are not sealed, boom joints, and the cooling ducts. The parasite drag coefficient for the tailless configuration is calculated to be approximately 0.018 and the parasite drag coefficient for the tail configuration is approximately 0.021. The larger

drag configuration, the tail configuration, will be used to assess the aircraft performance with each of the three propellers.

6.2 Thrust and Power Required

The thrust required for steady level flight for an aircraft is strictly a function of aircraft planform and is calculated using the following equation.

$$T_R = \frac{W}{C_L/C_D} \quad [15]$$

The available thrust is a function of the propeller/motor combination installed in the aircraft and is obtained from the analysis in Section 5.4.2 and Figure 49. Both the thrust required and the thrust available are plotted in the following figure.

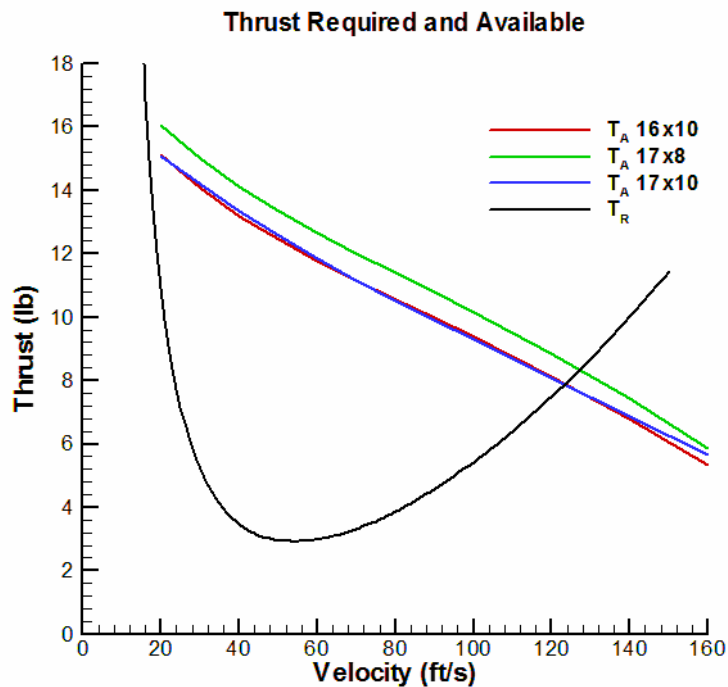


Figure 51: Thrust Required and Available

The velocity for minimum thrust required corresponds to the flight velocity for maximum L/D (maximum range) which for this aircraft is approximately 54 ft/s. The point at which the power available curve intersects (the higher velocity intersection) the power required curve corresponds to the maximum steady level speed for that particular propeller. The maximum velocity for the 16x10, 17x8, and 17x10 propellers are 124 ft/s, 127 ft/s, and 125 ft/s respectively with the 17x8 propeller selection producing the highest maximum steady level speed due to its higher overall thrust available.

The power required for the aircraft is obtained by multiplying the thrust required by the flight velocity; the power available is obtained the same way using the previously calculated thrust available Figure 49.

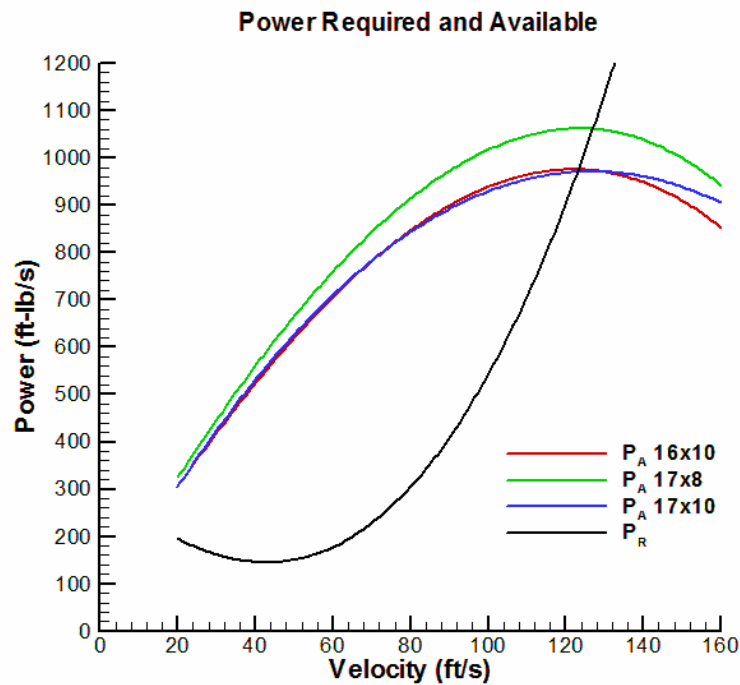


Figure 52: Power Required and Available

The velocity for minimum power required corresponds to flight speed for maximum endurance which is approximately 41 ft/s. Again the higher velocity intersection between the power required and power available curves corresponds to the maximum steady level velocity.

6.3 Rate of Climb

The rate of climb for the aircraft is a function of the excess power or the area between the power required and power available curves. The climb angle (γ) is found geometrically using the rate of climb and the velocity of the aircraft.

$$R/C = \frac{P_A - P_R}{W} \quad [16]$$

$$\gamma = \sin^{-1} \left(\frac{R/C}{V} \right) \quad [17]$$

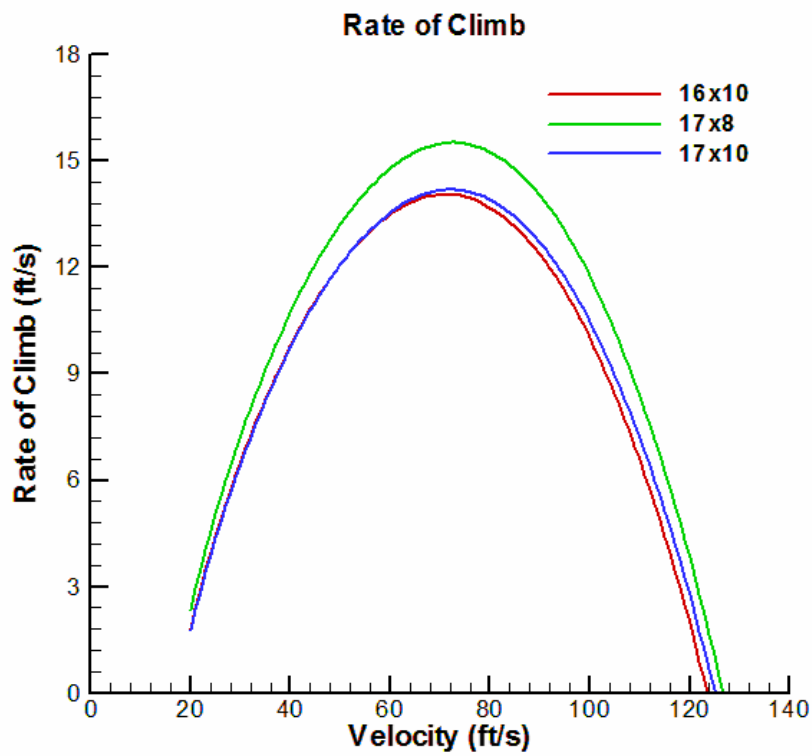


Figure 53: Rate of Climb

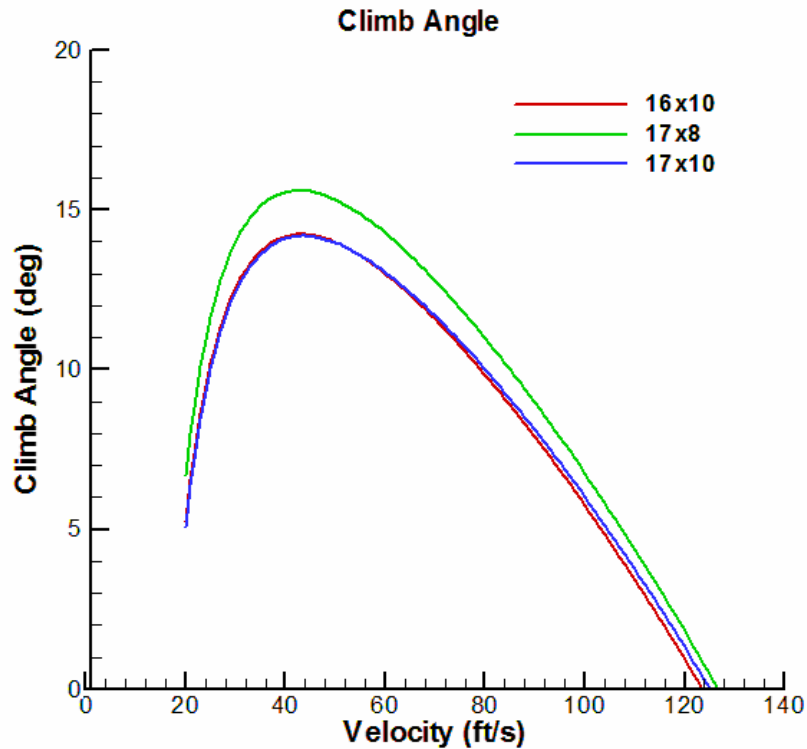


Figure 54: Climb Angle

Due to the relatively higher power available of the 17x8 propeller, it has a higher overall rate of climb than the other two propellers with a maximum rate of climb of 16 ft/s at an airspeed of 73 ft/s at 12 degrees. The 16x10 and 17x10 have essentially equal rate of climb characteristics for velocities below 60 ft/s with the 17x10 propeller having slightly larger rate of climb values for speed larger than 60 ft/s. The 17x10 propeller produces a maximum rate of climb of 14 ft/s at a velocity of 72 ft/s at 11 degrees, and the 16x10 propeller has a maximum rate of climb of 14 ft/s at a velocity of 71 ft/s at 11 degrees.

Rate of climb is especially important during initial climb-out after takeoff. The climb-out velocity for this aircraft is set to approximately $1.4 V_{\text{stall}}$ (62 ft/s). The rate of climb at climb-out velocity for the 17x10, 16x10, and 17x8 are 13.6 ft/s, 13.5 ft/s, and 14.8 ft/s respectively at climb angles of 13.0 degrees, 12.9 degrees, and 14.2 degrees respectively. The 17x8 propeller produces more desirable

climb performance compared to the other two propellers with a higher maximum rate of climb, climb-out rate of climb, and climb-out climb angle.

6.4 Range and Endurance

The range and endurance equations are simplified for this aircraft due to the fact that it is electrically powered and therefore has no change in weight due to fuel consumption. However, some assumptions must be made when accounting for this type of propulsion system. First, an efficiency for the motor/speed control combination must be estimated. This has been done by determining the power output from the battery and comparing it to the power absorbed by the propeller. The resulting power loss is attributed to inefficiencies in the motor, speed control, and wiring. The following table lists a sample of data points where the losses have been calculated.

Table 13: Electrical System Efficiency

Battery		Motor					
Volts	Amps	Power (Watts)	Power (ft-lb/s)	Torque (ft-lb)	RPM	Power	% loss
40.21	12.06	485	358	0.667	3975	278	0.22
40.11	11.63	467	344	0.671	3950	278	0.19
38.82	11.03	428	316	0.573	3975	239	0.24
38.66	17.89	692	510	0.981	4047	416	0.18
38.08	11.89	453	334	0.596	4243	265	0.21

A range of efficiencies from approximately 76% to 82% is observed for the data points taken. As a result, a conservative estimate of 76% electrical efficiency (η_e) will be used for the propulsion system.

The flight condition for maximum range occurs when the aircraft is operating at maximum L/D, or minimum thrust required. The velocity for this condition has been calculated previously to be 52 ft/s and the resulting thrust required at this velocity is approximately 2.9 lb. These two values can then be used to calculate the propeller thrust coefficient required as a function of advance ratio.

$$c_T = \frac{J^2 (T_R)_{\max \text{ range}}}{\rho d^2 (V_{\max \text{ range}})^2} \quad [18]$$

The thrust coefficient curve fit equations (Eq. 14) for each the three propellers are then equated to equation (Eq. 18) and solved for advance ratio. The equilibrium advance ratio is substituted into equation (Eq. 14) to determine the power coefficient which is then used to find the power required from the motor. The parameter values for operation at the velocity for maximum range are displayed in the following table.

Table 14: Maximum Range Operating Conditions

Propeller	J	n	c_T	c_P	$P_{\max \text{ range}}$
17x10	0.59	62 rev/s	0.079	0.074	239 ft-lb/s
16x10	0.57	69 rev/s	0.082	0.073	239 ft-lb/s
17x8	0.55	66 rev/s	0.069	0.059	236 ft-lb/s

The energy capacity of the batteries is found by multiplying the battery voltage and the battery capacity. During a given flight, the battery voltage will vary depending on current draw and elapsed flight time. However, the battery voltage should not be allowed to drop below the nominal voltage of the pack as this could result in damage to the battery. Thus, a conservative assumption of constant battery voltage equal to the nominal voltage is made. The nominal voltage for the 10 cell lithium polymer batteries is 37 volts and the capacity is 5 amp/hrs per battery pack resulting in 555 watt-hours of energy for the three packs in parallel. 20% of this energy capacity is reserved for the takeoff, climb, descent, and landing phases resulting in 444 watt-hours of capacity remaining. After converting the power required for maximum range to watts, the range (in feet) is calculated using the following equation and displayed in the following table.

$$R = \frac{\eta_e C_{batt}}{P} \cdot V \cdot 3600 \quad [19]$$

Table 15: Maximum Range

Propeller	Range	
16 x 10	194,000 ft	36.7 miles
17 x 8	198,000 ft	37.5 miles
17 x 10	194,000 ft	36.7 miles

The 17x10 and 16x10 propellers again produce similar performance with equal maximum range while the 17x8 produces the largest range.

A similar approach is used to determine the maximum endurance for each propeller. The velocity for maximum endurance was previously calculated to be 41 ft/s. However, this velocity is below the stall velocity of the aircraft. As a result, the velocity for maximum range (54 ft/s) will be used which is approximately $1.2 V_{stall}$. The following equation is used to calculate the endurance (in minutes) at this velocity.

$$E = \frac{\eta_{ps} C}{P_{max\ range}} \cdot 60 \quad [20]$$

Table 16: Maximum Endurance

Propeller	Endurance
16 x 10	63 mins.
17 x 8	64 mins.
17 x 10	63 mins.

6.5 Takeoff Performance

Takeoff performance is another important metric for propulsion system performance. The aircraft is required to be able to takeoff from Perkins Field which has a runway that is 454 feet long. The propulsion system must be able to accelerate the aircraft to liftoff velocity within the bounds of the runway. A MATLAB program (Appendix C) has been written to determine the takeoff distance and velocity of the aircraft with each of the three propellers. A numerical integration is applied using the Euler method to determine the instantaneous position, velocity, and acceleration of the aircraft.

The forces and moments considered are the lift, drag, and pitching moment of the aircraft; the propulsion system thrust; the normal and frictional forces on the landing gear wheels; and the weight of the aircraft.

The propulsion system is assumed to be at full throttle during the takeoff sequence, thus the previously calculated thrust available curves for each propeller are used. Because no experimental data has been acquired for velocities below approximately 18 ft/s, a thrust available value must be estimated for these velocities. It is assumed that the thrust for velocities below 18 ft/s is equal to the thrust value at 18 ft/s. This results in a conservative estimate as the thrust is expected to increase as the velocity decreases. For aircraft velocities above 18 ft/s the experimental data is used in the iteration.

The point of rotation is defined as the moment at which the normal force on the nose gear is zero. Once the aircraft reaches the rotation point the velocity and distance traveled are recorded. The program allows the user to select the magnitude of elevator deflection and velocity at which the elevator is applied; for these calculations the elevator is deflected -15 degrees at a velocity of 50 ft/s. These takeoff values have been calculated for the flying wing configuration and the configurations with the tail assembly and for each of the three propellers tested.

Table 17: Takeoff Rotation Distances and Velocities

	Rotate Distance	Rotate Velocity
Wing Only		
17x10	171 ft.	62 ft/s
16x10	171 ft.	
17x8	167 ft.	
Tail Configurations		
17x10	174 ft.	62 ft/s
16x10	174 ft.	
17x8	171 ft.	

All three propellers provide adequate rotate distance for operation at Perkins Field in both configurations. Again the performance of the 17x10 and 16x10 propellers are very similar due to the virtually equivalent thrust performance at these lower velocities. The rotate distances are

longer for the aft tail configuration due to the additional drag of the tail assembly. The 17x8 provides a shorter rotate distance for both configurations as a result of the relatively higher thrust available. The rotate velocity for both configurations is approximately $1.4 V_{\text{stall}}$.

6.6 Propeller Selection

According to the data collected and the analyses conducted, the 17x8 propeller provides superior performance in all criteria when compared to the 17x10 and 16x10 propellers. The lower pitch of the 17x8 propeller allows the motor to spin faster and the entire system to operate more efficiently. As a result, the propulsion system produces a larger amount of thrust and power available, a shorter takeoff distance, faster overall climb rate, and superior range and endurance when paired with the 17x8 propeller. Thus the 17x8 propeller is chosen to be paired with the AXi 5330/18 motor for the propulsion system in the Plank aircraft. The following table provides a summary of the aircraft performance using the 17x8 propeller.

Table 18: Aircraft Performance Summary with 17x8 Propeller

Parameter	Value
V_{max}	127 ft/s
Range	37.5 miles
Endurance	64 mins
Rotate Distance	171 ft
Rotate Velocity	62 ft/s
Max. Rate of Climb	15.5 ft/s

7. CONCLUSION

The Plank aircraft has been designed to meet the specifications set by the NASA Guidance and Controls Branch. The aircraft will serve as an experimental platform for the angular momentum bias flywheel. The aircraft has a re-configurable empennage with four separate configurations to allow for the momentum wheel to be tested against a variety of flying qualities. The design of the aircraft not only provides easy access to the momentum wheel and supporting components but also to all other components installed in the aircraft. An electric propulsion system has been chosen for the aircraft and will provide the operator with simple set-up, operation, and maintenance. Each of these aspects of the aircraft design will undoubtedly contribute to an efficient and successful flight test program of the bias angular momentum flywheel.

The Propeller Test Cell (PTC) has been designed to allow for experimental analysis of the Plank propulsion system. The PTC is capable of measuring the thrust and torque produced by the system along with the operating conditions of the motor, providing the operator the ability to fully characterize a given propulsion system. The re-configurability in the design and fabrication of the PTC will allow the operator to experimentally evaluate a large variety of propellers and motors in the NCSU Subsonic Wind Tunnel. The PTC has been calibrated and the resulting model error has been documented. A significant amount of work has been conducted to determine and mitigate sources of noise in the PTC including experimentally identifying the structural frequencies of the PTC.

The PTC was successfully used to evaluate the performance of three candidate four-blade propellers (16x10, 17x8, and 17x10) as well as the performance of the AXi 5330/18 motor. With this data, theoretical calculations were performed to evaluate expected aircraft performance parameters such as thrust and power available, rate of climb and angle of climb, range and endurance, and take off performance. Each of these parameters plays a vital role in the selection of a propulsion system and as such was used in selecting one of the three propellers for use on the constructed aircraft. The four-bladed 17x8 propeller has been determined to provide the most desirable aircraft performance and as such was chosen as the propeller for the Plank unmanned aerial vehicle.

8. FUTURE WORK:

Estimates have been made in this research for motor and propeller performance at maximum throttle. Initially, numerous issues arose when attempting to obtain experimental data at these conditions. A majority of these issues have been resolved including reconfiguring the wiring harness to withstand the necessary current and power, more accurately balancing the propeller assembly, and providing increased airflow to the motor and speed control. Future work would involve further attempts to obtain experimental data at maximum throttle in order to better predict thrust available and power available performance of the propulsion system.

The correction method currently used to adjust the thrust reading from the PTC load cell for temperature effects is a function of the residual thrust at the end of the run and the elapsed time for each data point. Future work could involve directly instrumenting the load cell for a temperature measurement(s) and developing a correlation equation between load cell temperature and the thermally induced thrust offset. This method would allow for real-time calculation of the thrust during testing and reduce the amount of post-processing required.

A larger variety of propellers can also be tested to provide more options for possible matches with the propulsion system. Propeller diameters of up to 18 inches can be used on this aircraft due to clearance between the tailbooms. Diameters of 18 inches were initially planned to be tested in this research, however, the four-bladed 18 inch propellers produced by Zinger had a 3.5 inch hub making it too large to fit in the 3.5 inch spinner. Zinger recently reduced the size of the hub for their 18 inch propellers to 2.5 inches. This larger propeller diameter can now be tested with pitches of 5, 6, 8, and 10 inches using the procedures outlined in this research.

REFERENCES:

¹E-works.cz. (2008). *AXI 5330/18 Gold Line*. Retrieved Aug. 8, 2008, from Model Motors, Czech Republic. Web site:

<http://www.modelmotors.cz/index.php?page=61&product=5330&serie=18&line=GOLD>.

²Castle. (2006). *Phoenix HV High Voltage Brushless Motor Controls*. Retrieved Aug. 8, 2008, from Castle Creations, Olathe, Kansas. Web site:

http://www.castlecreations.com/products/phoenix_hv_series.html.

³Automation Creations. (2008). *MatWeb Material Property Data*. Retrieved Mar. 25, 2008, from Automation Creations, Inc., Blacksburg, VA. Web site: <http://www.matweb.com/index.aspx>.

⁴Vishay Micro-Measurements EA-13-031DE-350/E Strain Gage Package Documentation

⁵Vishay Micro-Measurements EA-13-060LZ-120/E Strain Gage Package Documentation

⁶Kline, S. J., and McClintock, F. A. (1953). *Describing Uncertainties in Single Sample Experiments*. Mechanical Engineering, **75**, p. 3.

⁷Fitzgerald, R E. (2007). *Wind Tunnel Blockage Corrections for Propellers*. College Park, MD: University of Maryland.

⁸Glauert, H. (1930). *The Elements of Aerofoil and Airscrew Theory*. Fetter Lane, London: Cambridge University Press.

⁹Weick, F E. (1930). *Aircraft Propeller Design*. New York: McGraw-Hill. p. 95.

¹⁰Drela, M. (2007). *First-Order DC Electric Motor Model*. Retrieved July 1, 2009, from MIT Aeronautics and Astronautics, Cambridge, MA. Web site: http://web.mit.edu/drela/Public/web/qprop/motor1_theory.pdf.

¹¹Raymer, D P. (2006). *Aircraft Design: A Conceptual Approach*. Reston, VA: American Institute of Aeronautics and Astronautics.

APPENDICES

Appendix A: Calibration Run Schedule

Table 19: Calibration Run Schedule

Run #	Pattern	Thrust lb	Torque ft-lb	Weight lb
1	133	0	1.819	0.882
2	321	30	0.909	0
3	222	15	0.909	0.441
4	233	15	1.819	0.882
5	0	15	0.909	0.441
6	0	15	0.909	0.441
7	311	30	0.000	0
8	113	0	0.000	0.882
9	0	15	0.909	0.441
10	0	15	0.909	0.441
11	122	0	0.909	0.441
12	121	0	0.909	0
13	332	30	1.819	0.441
14	213	15	0.000	0.882
15	0	15	0.909	0.441
16	123	0	0.909	0.882
17	132	0	1.819	0.441
18	111	0	0.000	0
19	0	15	0.909	0.441
20	0	15	0.909	0.441
21	211	15	0.000	0
22	322	30	0.909	0.441
23	231	15	1.819	0
24	323	30	0.909	0.882
25	0	15	0.909	0.441
26	0	15	0.909	0.441
27	212	15	0.000	0.441

28	232	15	1.819	0.441
29	331	30	1.819	0
30	0	15	0.909	0.441
31	0	15	0.909	0.441
32	221	15	0.909	0
33	0	15	0.909	0.441
34	123	0	0.909	0.882
35	313	30	0.000	0.882
36	312	30	0.000	0.441
37	112	0	0.000	0.441
38	0	15	0.909	0.441
39	131	0	1.819	0
40	311	30	0.000	0
41	0	15	0.909	0.441
42	121	0	0.909	0
43	322	30	0.909	0.441
44	333	30	1.819	0.882
45	232	15	1.819	0.441
46	0	15	0.909	0.441
47	112	0	0.000	0.441
48	0	15	0.909	0.441
49	221	15	0.909	0
50	331	30	1.819	0
51	323	30	0.909	0.882
52	312	30	0.000	0.441
53	222	15	0.909	0.441
54	0	15	0.909	0.441
55	211	15	0.000	0
56	0	15	0.909	0.441
57	0	15	0.909	0.441
58	131	0	1.819	0
59	313	30	0.000	0.882

60	132	0	1.819	0.441
61	223	15	0.909	0.882
62	212	15	0.000	0.441
63	122	0	0.909	0.441
64	233	15	1.819	0.882
65	133	0	1.819	0.882
66	213	15	0.000	0.882
67	113	0	0.000	0.882
68	333	30	1.819	0.882
69	0	15	0.909	0.441
70	321	30	0.909	0
71	332	30	1.819	0.441
72	231	15	1.819	0
73	111	0	0.000	0
74	223	15	0.909	0.882

Appendix B: Wind Tunnel Data

Table 20: 16x10 Propeller Data

V (ft/s)	J	RPM	Thrust (lb)	Torque (ft-lb)	Power (ft-lb/s)	Ct	Cp	Cs	η
18.2	0.206	3975	5.09	0.677	281.9	0.159	0.100	0.360	0.328
23.2	0.263	3975	4.77	0.671	279.4	0.149	0.099	0.450	0.397
27.3	0.309	3975	4.56	0.664	276.5	0.143	0.098	0.522	0.450
33.5	0.379	3975	4.18	0.652	271.6	0.131	0.096	0.633	0.515
38.7	0.441	3950	3.67	0.611	252.6	0.116	0.091	0.737	0.562
43.9	0.501	3950	3.09	0.560	231.6	0.098	0.084	0.844	0.586
49.1	0.560	3950	2.49	0.496	205.0	0.079	0.074	0.959	0.597
54.3	0.619	3950	1.97	0.435	180.1	0.063	0.065	1.083	0.593
59.5	0.678	3950	1.35	0.357	147.5	0.043	0.053	1.229	0.545
59.6	0.678	3950	1.37	0.367	152.0	0.044	0.055	1.222	0.537
54.3	0.615	3975	1.96	0.438	182.2	0.062	0.065	1.078	0.585
49.2	0.557	3975	2.58	0.503	209.3	0.081	0.074	0.954	0.606
43.9	0.497	3975	3.20	0.573	238.4	0.101	0.085	0.835	0.589
38.6	0.437	3975	3.76	0.616	256.3	0.118	0.091	0.731	0.568
33.5	0.379	3975	4.16	0.644	268.2	0.131	0.095	0.634	0.519
28.5	0.322	3975	4.49	0.662	275.6	0.141	0.098	0.543	0.464
23.4	0.264	3975	4.76	0.670	278.7	0.150	0.099	0.452	0.399
18.1	0.204	3975	5.00	0.674	280.4	0.157	0.100	0.358	0.322
18.0	0.198	4100	5.44	0.708	304.0	0.161	0.098	0.315	0.323
23.2	0.255	4100	5.20	0.703	301.8	0.154	0.098	0.406	0.400
28.3	0.310	4100	4.95	0.698	299.7	0.146	0.097	0.495	0.467
33.4	0.367	4100	4.62	0.684	293.6	0.136	0.095	0.587	0.526
38.6	0.424	4100	4.16	0.651	279.3	0.123	0.091	0.685	0.575
43.8	0.480	4100	3.63	0.601	258.1	0.107	0.084	0.789	0.616
48.9	0.537	4100	3.04	0.543	233.3	0.090	0.076	0.900	0.638

54.2	0.595	4100	2.49	0.481	206.4	0.074	0.067	1.021	0.654
59.4	0.652	4100	1.90	0.413	177.2	0.056	0.058	1.154	0.638
64.6	0.710	4100	1.22	0.319	136.8	0.036	0.045	1.322	0.578
64.6	0.709	4100	1.20	0.318	136.4	0.036	0.044	1.322	0.568
59.4	0.652	4100	1.85	0.410	175.9	0.055	0.057	1.155	0.624
54.2	0.595	4100	2.51	0.490	210.5	0.075	0.069	1.016	0.647
49.0	0.538	4100	3.11	0.554	237.8	0.092	0.078	0.896	0.640
43.8	0.480	4100	3.67	0.610	262.0	0.109	0.085	0.786	0.614
38.6	0.424	4100	4.22	0.658	282.5	0.125	0.092	0.683	0.577
33.4	0.367	4100	4.68	0.689	295.9	0.139	0.096	0.586	0.528
28.3	0.310	4100	5.00	0.706	303.1	0.149	0.099	0.493	0.467
23.1	0.253	4100	5.16	0.703	302.0	0.153	0.098	0.403	0.394
18.1	0.199	4100	5.38	0.706	303.3	0.160	0.099	0.316	0.322

Table 21: 17x8 Wind Tunnel Data

V (ft/s)	J	RPM	Thrust (lb)	Torque (ft-lb)	Power (ft-lb/s)	Ct	Cp	Cs	η
17.8	0.184	4100	6.41	0.860	368.5	0.148	0.088	0.299	0.309
22.8	0.235	4100	6.04	0.859	368.9	0.139	0.088	0.383	0.373
28.1	0.290	4100	5.96	0.838	359.6	0.138	0.086	0.474	0.465
33.2	0.343	4100	5.02	0.811	347.0	0.116	0.083	0.564	0.479
38.4	0.397	4100	4.51	0.777	333.0	0.104	0.080	0.658	0.519
43.6	0.451	4100	4.23	0.729	312.5	0.098	0.075	0.757	0.590
48.7	0.504	4100	3.78	0.665	286.1	0.088	0.068	0.861	0.646
54.0	0.558	4100	2.95	0.566	243.1	0.068	0.058	0.985	0.656
59.3	0.613	4100	2.15	0.476	205.2	0.050	0.049	1.119	0.623
64.5	0.666	4100	1.29	0.368	158.2	0.030	0.038	1.282	0.526
69.8	0.721	4100	0.39	0.254	109.2	0.009	0.026	1.493	0.247
64.8	0.669	4100	0.89	0.365	157.5	0.021	0.038	1.287	0.369

59.4	0.614	4100	2.02	0.476	205.2	0.047	0.049	1.120	0.589
54.1	0.559	4100	2.86	0.570	245.3	0.067	0.059	0.985	0.633
48.8	0.505	4100	3.61	0.654	281.0	0.084	0.068	0.865	0.628
43.6	0.450	4100	4.37	0.736	318.0	0.102	0.076	0.753	0.602
38.4	0.397	4100	4.97	0.783	337.1	0.116	0.081	0.656	0.568
33.2	0.343	4100	5.44	0.807	345.2	0.127	0.083	0.564	0.521
28.0	0.289	4100	5.90	0.835	357.5	0.137	0.086	0.472	0.461
22.8	0.235	4100	6.22	0.847	362.9	0.145	0.087	0.383	0.390
17.7	0.183	4100	6.46	0.851	363.4	0.150	0.087	0.298	0.313
17.8	0.185	4075	6.60	0.850	362.7	0.154	0.088	0.300	0.323
22.8	0.237	4075	6.30	0.841	359.0	0.147	0.087	0.385	0.400
28.0	0.291	4075	5.97	0.834	355.9	0.140	0.087	0.475	0.469
33.2	0.343	4100	5.50	0.808	347.1	0.127	0.083	0.564	0.525
38.3	0.396	4100	4.89	0.762	327.1	0.113	0.078	0.659	0.573
43.6	0.450	4100	4.31	0.718	308.1	0.100	0.074	0.759	0.610
48.9	0.505	4100	3.57	0.646	277.2	0.083	0.066	0.868	0.630
54.0	0.558	4100	2.85	0.563	241.6	0.066	0.058	0.987	0.638
59.4	0.614	4100	2.03	0.465	199.6	0.047	0.048	1.128	0.604
64.6	0.668	4100	1.20	0.361	155.1	0.028	0.037	1.290	0.501
64.7	0.668	4100	1.18	0.361	155.0	0.027	0.037	1.290	0.492
59.3	0.613	4100	2.06	0.474	203.7	0.048	0.049	1.120	0.600
54.1	0.559	4100	2.85	0.572	245.7	0.066	0.059	0.984	0.628
48.8	0.504	4100	3.57	0.648	278.3	0.083	0.067	0.865	0.625
43.7	0.451	4100	4.23	0.717	307.9	0.098	0.074	0.759	0.599
38.4	0.396	4100	4.94	0.773	331.9	0.115	0.080	0.657	0.571
33.2	0.343	4100	5.49	0.816	350.3	0.128	0.084	0.562	0.520
27.9	0.288	4100	5.87	0.832	357.2	0.136	0.086	0.471	0.459
22.7	0.235	4100	6.23	0.847	363.5	0.145	0.087	0.383	0.390
17.7	0.183	4100	6.58	0.853	366.1	0.153	0.088	0.297	0.318

Table 22: 17x10 Wind Tunnel Data

V (ft/s)	J	RPM	Thrust (lb)	Torque (ft-lb)	Power (ft-lb/s)	Ct	Cp	Cs	η
18.5	0.193	4060	7.20	0.981	417.2	0.170	0.103	0.304	0.360
24.0	0.251	4045	6.69	0.969	410.5	0.159	0.102	0.396	0.427
29.4	0.309	4025	6.34	0.957	403.3	0.152	0.102	0.488	0.495
34.1	0.358	4025	5.95	0.939	395.8	0.143	0.100	0.568	0.541
38.1	0.401	4025	5.60	0.915	385.9	0.135	0.098	0.639	0.580
43.1	0.450	4060	5.09	0.879	373.7	0.120	0.092	0.725	0.610
48.5	0.501	4100	4.61	0.832	357.2	0.107	0.086	0.819	0.644
54.4	0.557	4135	4.02	0.773	334.7	0.092	0.078	0.928	0.667
60.1	0.608	4185	3.40	0.705	309.2	0.076	0.070	1.036	0.672
64.5	0.647	4225	2.89	0.647	286.3	0.063	0.063	1.124	0.658
68.7	0.682	4265	2.38	0.585	261.5	0.051	0.056	1.215	0.633
73.6	0.721	4325	1.86	0.514	232.7	0.039	0.048	1.325	0.594
77.9	0.754	4375	1.37	0.446	204.5	0.028	0.041	1.431	0.524
74.6	0.728	4335	1.78	0.494	224.4	0.037	0.046	1.349	0.595
67.3	0.672	4240	2.58	0.596	264.7	0.056	0.058	1.188	0.663
61.4	0.623	4175	3.27	0.669	292.6	0.074	0.067	1.069	0.696
54.0	0.558	4100	4.00	0.751	322.4	0.093	0.078	0.930	0.685
43.2	0.454	4025	5.09	0.840	353.9	0.123	0.090	0.735	0.644
35.1	0.374	3980	5.78	0.894	372.5	0.143	0.098	0.595	0.575
27.7	0.296	3950	6.34	0.913	377.6	0.160	0.102	0.468	0.500
18.1	0.195	3935	6.85	0.915	376.9	0.174	0.103	0.307	0.372
8.3	0.112	3150	4.57	0.577	190.3	0.181	0.101	0.177	0.248
17.6	0.182	4100	7.47	1.012	434.6	0.172	0.103	0.287	0.303

22.7	0.235	4100	7.08	1.000	429.4	0.163	0.102	0.370	0.374
27.8	0.287	4100	6.70	0.990	425.2	0.154	0.101	0.454	0.438
33.0	0.340	4100	6.31	0.979	420.4	0.146	0.100	0.540	0.495
38.2	0.395	4100	5.79	0.946	406.0	0.134	0.097	0.629	0.545
43.3	0.447	4100	5.09	0.887	380.8	0.118	0.091	0.723	0.579
48.5	0.501	4100	4.49	0.833	357.7	0.104	0.085	0.820	0.609
53.8	0.556	4100	3.78	0.759	326.0	0.087	0.078	0.926	0.623
59.0	0.610	4100	3.06	0.676	290.3	0.071	0.069	1.040	0.622
64.4	0.665	4100	2.31	0.587	251.9	0.054	0.060	1.166	0.591
69.7	0.720	4100	1.52	0.476	204.3	0.035	0.049	1.316	0.519
69.6	0.719	4100	1.48	0.472	202.7	0.034	0.049	1.317	0.508
64.4	0.665	4100	2.34	0.590	253.5	0.054	0.061	1.164	0.595
59.1	0.607	4125	3.08	0.676	292.1	0.071	0.069	1.036	0.624
53.9	0.553	4125	3.79	0.762	329.0	0.087	0.078	0.922	0.621
48.6	0.499	4125	4.56	0.839	362.6	0.105	0.085	0.815	0.611
43.3	0.445	4125	5.14	0.895	386.6	0.118	0.091	0.718	0.576
38.2	0.392	4125	5.87	0.948	409.4	0.135	0.096	0.626	0.547
33.0	0.338	4125	6.24	0.973	420.3	0.143	0.099	0.537	0.489
27.8	0.286	4125	6.68	0.999	431.6	0.153	0.102	0.451	0.430
22.8	0.234	4125	6.91	1.002	433.0	0.158	0.102	0.369	0.363
17.6	0.181	4125	7.18	1.001	432.6	0.165	0.102	0.286	0.293

Appendix C: Take Off MATLAB Code (Takeoff_Master.m)

```
%%%%%%%%%%%%%%%%%%%%%%%%%%%%%%%%%%%%%%%%%%%%%%%%%%%%%%%%%%%%%%%%%%%%%%%%
%
%                               TAKE OFF ANALYSIS                               %
%%%%%%%%%%%%%%%%%%%%%%%%%%%%%%%%%%%%%%%%%%%%%%%%%%%%%%%%%%%%%%%%%%%%%%%%

% Plank Project
% Jason Bishop
% Apr. 2009

clear
clc
close all

% This program uses an integral method to determine the takeoff
% performance of the Plank aircraft.

% Note:
% Initial steps have been taken to incorporate the rotation of the
% aircraft up to the point of lift-off. However, translation of the cg
% due to aircraft rotation needs to be accounted for in the calculations.

% English Units (ft,lb,s)
%%
% Reference Conditions

choice = 2 ;    % 1 = Flying Wing; 2 = Aft Tail

prop = 3 ;      % 1 = 17x10 ; 2 = 16x10 ; 3 = 17x8
de_c = -15 ;    % commanded elevator position
V_e = 50 ;      % velocity of elevator application

rho = 0.00238 ; % Density
g = 32.2 ;      % Gravity
S = 20 ;        % Reference Area
cbar = 2 ;      % Reference Chord
W = 40 ;        % Weight
dm = 1/12 ;     % motor vertical offset
dw = 5.5/12 ;   % wheel diameter
mu_r = 0.04 ;   % coefficient of rolling friction
a = 3/180*pi ;

if choice == 1
    Iyy = 1.3 ;    % Flying wing Pitch moment of inertia (slug*ft^2)
    xcg = 0.395 ; % Flying Wing CG Location
elseif choice == 2
    Iyy = 2.43 ;   % Aft Tail Pitch moment of inertia (slug*ft^2)
    xcg = 0.52 ;   % Aft Tail CG Location
else
    disp(sprintf('Inappropriate Configuration Choice'))
    Iyy = 0 ;
    xcg = 100 ;
end
```

```

end

%%
% Landing Gear Geometry

xn = -16 /12 ; % nose gear location
xm = 8.7 /12 ; % main gear location
h = 11.7 /12 ; % height of main gear strut
xm = xm - h*a ;

%%
% Location Vectors
% [0,0,0] = wing vertex
% +x: aft, +y: right, +z up

rp = [xm,0,-h] ; % Pivot Point (main gear axle)
rw = [2.5*0.25,0,0] ; % Wing A/C
rcg = [xcg,0,0] ; % Center of Gravity
rt = [0,0,dm] ; % Thrust line
rm = [xm,0,-(h+dw/2)] ; % Main gear contact point
rn = [xn,0,-(h+dw/2)] ; % Nose gear contact point

% Vectors from Pivot
rpw = rw - rp ;
rpcg = rcg - rp ;
rpt = rt - rp ;
rpm = rm - rp ;
rpn = rn - rp ;

%%
% Aircraft
e = 0.95 ;
AR = 5 ;
phi = 1 ;

if choice == 1
    % Stability Derivatives for Wing Only
    % * all coefficients in ground effect
    CLo = -0.0174 ;
    CLa = 3.9194 ;
    CLde = 0.022563 ; % in /deg
    CLq = 5.165138 ;
    CMo = 0.0210 ;
    CMa = -0.398551 ;
    CMde = -0.008449 ; % in /deg
    CMq = -1.335606 ;
    CDo = 0.018 ;
elseif choice == 2
    % Stability Derivatives for Aft Tail
    % * all coefficients in ground effect
    CLo = -0.0174 ;
    CLa = 4.005 ;
    CLde = 0.022076 ; % in /deg
    CLq = 5.565 ;
    CMo = 0.0210 ;

```

```

    CMa = -0.4076 ;
    CMde = -0.006510 ; % in /deg
    CMq = -2.8601 ;
    CDo = 0.021 ;
else
    disp(sprintf('Inappropriate Configuration Choice'))
end
% Aero Coefficients
CL = @(a,q,de) CLo + CLa*(a) + CLde*(de) + CLq*(q);
CD = @(a,q,de) phi*CL(a,q,de)^2/(pi*e*AR) + CDo;
CM = @(a,q,de) CMo + CMa*(a) + CMde*(de) + CMq*(q);

% Initialize variables of motion
s = 0 ; % displacement
V = 0 ; % velocity
dV = 0 ; % acceleration
t1 = 0 ; % initial time (seconds)
ts = 0.01 ; % time step
t2 = 30 ; % final time

th = 0 ;
thd = 0 ;
q = 0 ;
de = 0 ; % elevator deflection in degrees
i = 1 ;

Vr = ones(1,(t2-t1)/ts)+1000 ;
sr = ones(1,(t2-t1)/ts)+1000 ;

for t = t1:ts:t2

    Q = 0.5*rho*V^2 ;

    % Forces
    L = Q*S*CL(a,q,de) ;
    D = Q*S*CD(a,q,de) ;
    M = Q*S*cbar*CM(a,q,de) ;

    % Curve fit from thrust available calcs
    Ta_1710 = -0.065*V + 15.96 ;
    Ta_1610 = -0.066*V + 15.98 ;
    Ta_178 = -0.069*V + 17.01 ;

    % thrust values for low speeds outside of test data
    if V <= 18
        Ta_1710 = 14.8 ;
        Ta_1610 = 14.8 ;
        Ta_178 = 15.8 ;
    end

    % Assign Ta for propeller choice
    if prop == 1
        Ta = -1*Ta_1710 ;
    elseif prop == 2

```

```

    Ta = -1*Ta_1610 ;
elseif prop == 3
    Ta = -1*Ta_178 ;
else
    disp(sprintf('Inappropriate Propeller Choice'))
    Ta = 0 ;
end

% L = 0 ;
% D = 0 ;
% M = 0 ;
% Ta = 0 ;
% a = 0 ;

% make forces into vectors
vL = [L*sin(a),0,L*cos(a)] ;
vD = [D*cos(a),0,-D*sin(a)] ;
vM = [0,M,0] ;
vW = [0,0,-W] ;
vT = [Ta*cos(a),0,-Ta*sin(a)] ;

% Find forces on gear
% sum moments about pivot to find force on nose gear
sM = cross(rpw,vL) + cross(rpw,vD) + M + cross(rpt,vT) + ...
    cross(rpcg,vW) ;
Fn = sM(2)/rpn(1) ;
if Fn < 0
    Fn = 0 ;
    Vr(i) = V ;
    sr(i) = s ;
end
vFn = [0 0 Fn] ;

% sum forces in z to find force on main gear
sFz = vL(3) + vD(3) + vW(3) + vT(3) + vFn(3) ;
Fm = -sFz ;
vFm = [0 0 Fm] ;

% Calc frictional forces
fFn = Fn*mu_r ;
fFm = Fm*mu_r ;

% Sum forces in x-direction
Fx = -(vL(1) + vD(1) + vT(1) - fFm - fFn) ;

% Equations of Motion
% Linear
dV = Fx/(W/g) ; % Newton's second
s = s + V*ts + 0.5*dV*ts^2 ;
V = V + dV*ts ;

% Sum of moments about y-axis

```

```

My = dot(sM + cross(rpn,vFn),[0 1 0]) ;
% Rotational
thdd = My/Iyy ;
th = a + thd*ts + 0.5*thdd*ts^2 ;
thd = thd + thdd*ts ;

a = th ; % update angle of attach theta=alpha
q = thd ; % update angular velocity

% Debug
ta(i) = t ;
sa(i) = s ;
aa(i) = a*180/pi ;
qa(i) = q ;
Va(i) = V ;
Fna(i) = Fn ;
La(i) = vL(3) ;
Ma(i) = M ;
Taa(i) = Ta ;
i = i + 1 ;

% Rotating when no weight on nose gear
if Fn == 0
    disp('Rotate')
    %break
end

% Liftoff when lift is greater than weight
if L > W
    disp('Liftoff')
    break
end

if V > V_e
    de = de_c ;
end
end

%%
% Display and Plotting

disp(sprintf('\tElevator Angle :\t%4.1f\tdeg.',de))
disp(sprintf('\tRotate Distance :\t%4.1f\tft.',min(sr)))
disp(sprintf('\tRotate Velocity :\t%4.1f\tft/s ',min(Vr)))
disp(sprintf('\tTakeoff Distance :\t%4.1f\tft.',s))
disp(sprintf('\tLiftoff Velocity :\t%4.1f\tft/s ',V))

% Displacement
subplot(2,3,1)
plot(ta,sa)
xlabel('Time (seconds)')
ylabel('Displacement (ft)')

subplot(2,3,2)

```

```
plot(ta,Va)
xlabel('Time (seconds)')
ylabel('Velocity (ft/s)')

subplot(2,3,3)
plot(ta,aa)
xlabel('Time (seconds)')
ylabel('Angle of Attack (deg)')

subplot(2,3,4)
plot(ta,Fna)
xlabel('Time (seconds)')
ylabel('Force on Nose Gear (lbs)')

subplot(2,3,5)
plot(ta,La)
xlabel('Time (seconds)')
ylabel('Lift (lb)')

subplot(2,3,6)
plot(ta,qa)
xlabel('Time (seconds)')
ylabel('Angular Velocity (rad/s)')
```